1990

Two-Dimensional ^{1}H and ^{31}P NMR Spectra and Restrained Molecular Dynamics Structure of an Oligodeoxyribonucleotide Duplex Refined via a Hybrid Relaxation Matrix Procedure

Robert Powers
University of Nebraska - Lincoln, rpowers3@unl.edu

Claude R. Jones
Purdue University

David G. Gorenstein
Purdue University

Published in *Journal of Biomolecular Structure and Dynamics* 8:2 (1990), pp. 253–294;
doi: 10.1080/07391102.1990.10507805.

Submitted June 6, 1990; published online May 21, 2012.

Two-Dimensional ^{1}H and ^{31}P NMR Spectra and Restrained Molecular Dynamics Structure of an Oligodeoxyribonucleotide Duplex Refined via a Hybrid Relaxation Matrix Procedure

Robert Powers, Claude R. Jones, and David G. Gorenstein

Department of Chemistry, Purdue University, West Lafayette, Indiana 47907 USA

Abstract

Assignment of the ^{1}H and ^{31}P resonances of a decamer DNA duplex, d(CGCTTAAGCG)$_2$ was determined by two-dimensional COSY, NOESY, and ^{1}H-^{31}P *P*ure *A*bsorption phase *C*onstant time (PAC) heteronuclear correlation spectroscopy. The solution structure of the decamer was calculated by an iterative hybrid relaxation matrix method combined with NOESY-distance restrained molecular dynamics. The distances from the 2D NOESY spectra were calculated from the relaxation rate matrix which were evaluated from a hybrid NOESY volume matrix comprising elements from the experiment and those calculated from an initial structure. The hybrid matrix-derived distances were then used in a restrained molecular dynamics procedure to obtain a new structure that better approximates the NOESY spectra. The resulting partially refined structure was then used to calculate an improved theoretical NOESY volume matrix which is once again merged with the experimental matrix until refinement is complete. $J_{H3'-P}$ coupling constants for each of the phosphates of the decamer were obtained from ^{1}H-^{31}P J-resolved selective proton flip 2D spectra. By using a modified Karplus relationship the C4′-C3′-O3′-P torsional angles (ε) were obtained. Comparison of the ^{31}P chemical shifts and $J_{H3'-P}$ coupling constants of this sequence has allowed a greater insight into the various factors responsible for ^{31}P chemical shift variations in oligonucleotides. It also provides an important probe of the sequence-dependent structural variation of the deoxyribose phosphate backbone of DNA in solution. These correlations are consistent with the hypothesis that changes in local helical structure perturb the deoxyribose phosphate backbone. The variation of the ^{31}P chemical shift, and the degree of this variation from one base step to the next is proposed as a potential probe of local helical conformation within the DNA double helix. The pattern of calculated ε and ζ torsional angles

from the restrained molecular dynamics refinement agrees quite well with the measured $J_{H3'-P}$ coupling constants. Thus, the local helical parameters determine the length of the phosphodiester backbone which in turn constrains the phosphate in various allowed conformations.

Introduction

Nuclear magnetic resonance methods have developed as powerful probes of the structure and dynamics of DNA fragments in solution (1–4). The development of sequence-specific, two-dimensional nuclear magnetic resonance (2D NMR) assignment methodologies (5–14) and higher-field spectrometers have made the study of modest size oligonucleotides (10–20 base pairs) possible. Two-dimensional NMR, combined with distance geometry (15–17) or restrained molecular mechanics/dynamics (3–20), is now capable of elucidating the fine structure of short DNA duplexes in solution. Unfortunately, evaluation of interproton distances from a 2D-NMR nuclear Overhauser effect spectroscopy (NOESY) experiment has relied on the so-called "two-spin approximation" (17, 21). The approximation requires that the NOESY-derived distances be obtained from vanishingly short experimental mixing times where the rate of build-up of the NOE crosspeak intensity is ca. linear and the effects of spin diffusion (NOE intensity mediated by multiple relaxation pathways) are minimal. Because most of the structurally important longer range NOEs are not observed at these short mixing times, the use of the two-spin approximation has raised concern over the validity of highly refined NMR structures derived by this methodology (3, 4, 20, 22). In order to obtain more accurate distances we have invoked the use of a complete relaxation matrix approach for solving the Bloch equations of magnetization. The matrix approach removes the effects of spin diffusion, which allows for the measurement of interproton distance with a higher degree of precision and accuracy (3, 20, 23). A very promising approach to NMR structural refinement involves the direct calculation of the NOESY rate matrix (and hence distances) from the experimental NOESY volume matrix (3, 20, 22, 24). However, the use of the relaxation matrix method is sensitive to the completeness of the experimental NOESY data. One solution to this problem is provided by a "hybrid matrix approach" (see also ref. 25 for an alternative solution to this problem).

The hybrid matrix approach (3, 20, 26, 27, 28) addresses the problem of incomplete experimental data by combining the information from the experimental NOESY volumes, v_{ij}^{exp}, and calculated volumes, v_{ij}^{c}, which is dependent upon the cross-relaxation rate between spins i and j, to generate a hybrid volume matrix, V^{hyb}. The v_{ij}^{c} matrix elements are initially derived from a structure refined from a two-spin analysis of the NOESY data. The hybrid volume matrix is then used to evaluate the rate matrix, whose off-diagonal elements include the effects of spin diffusion. The distances derived from this hybrid relaxation rate matrix are then utilized as constraints in a restrained molecular dynamics simulation. This process is repeated until a satisfactory agreement between the calculated and observed crosspeak volumes is obtained. This hybrid matrix methodology provides a very powerful means to automate the refinement process for deriving solution structures from NMR data. This refinement procedure has allowed us to accurately extract interproton distances, which are not obtainable using the two-spin approximation, which is nearly universally used in other 2D NOESY NMR structural analyses.

^{1}H/^{1}H 2D NOESY spectra give no direct information on the sugar phosphate conformation, and NOESY distance-constrained structures have been suggested to be effectively disordered in this part of the structure (4). However, ^{31}P chemical shifts and ^{1}H-^{31}P coupling constants can provide valuable information on the phosphate ester backbone conformation (29). A major limitation in the use of ^{31}P NMR in providing information on the backbone conformation has been the difficulty in assigning the ^{31}P resonances. Fortunately, newer reverse detection (30) and long-range, constant time HETCOR (31, 32) methods have now been successfully applied to the ^{31}P assignment problem.

One of the main reasons for assigning ^{31}P resonances of oligonucleotides is to obtain information on the conformation of the phosphodiester backbone. (29, 33–35). Theoretical studies have shown that of the six torsional angles that define the sugar phosphate backbone, the conformation of the α: O3′-P-O5′-C5′ and ζ: C3′-O3′-P-O5′ torsional angles appear to be most important in determining the ^{31}P chemical shifts (29, 35, 36).

In duplex B-DNA, the gauche(–), gauche(–) (g^-, g^-; ζ, α) conformation[1] of the phosphate ester backbone is energetically favored, and this conformation is associated with a more shielded ^{31}P resonance. In single-stranded DNA, the trans, gauche(–) (t, g^-) conformation (as well as other staggered conformations about the P--O ester bonds) is also significantly populated due to the added flexibility of the random coil phosphodiester backbone. The ^{31}P signal of the random coil state is shifted downfield relative to that of the duplex DNA (37, 38). The ^{31}P chemical shift difference between the two g^-, g^- and t, g^- conformational states is estimated to be 1.5–1.6 ppm (33, 39).

Initial studies on duplex oligonucleotides have shown that ^{31}P chemical shifts are dependent upon position of the phosphate residue as well as sequence (33, 35, 37, 40). That is, the more centralized the phosphate is within the oligonucleotide duplex the more upfield is its associated ^{31}P chemical shift; this is referred to as the "positional relationship." Thus, the phosphodiester conformation becomes more g^-, g^- as the phosphate positions become more centrally located in the sequence, reaching a point where the linkage conformation is expected to be fully polymeric in character (g^-, g^- P-O ester conformation). There appears to be a sequence-specific effect on ^{31}P chemical shifts as well. As described in more detail below, local helical distortions arise along the DNA chain due to purine-purine steric clash on opposite strands of the double helix (41, 42). A modest correlation exists between the local helical parameters such as helix twist or roll angle and ^{31}P chemical shifts (36, 43–45).

In this paper we analyze the sequence-specific and positional-specific variations in the ^{31}P chemical shifts and $J_{H3'-P}$ coupling constants of the $(CGCTTAAGCG)_2$ decamer duplex. This has provided information on the backbone conformation of the B-DNA structure in solution. We demonstrate that there exists a good correlation between the backbone torsional angles ε and ζ with ^{31}P chemical shifts. In addition, the solution structure was refined by a hybrid matrix/NOESY-distance restrained molecular dynamics methodology (3, 20, 28, 46). While the 2D NOESY spectra gave no direct information on the sugar phosphate conformation, we demonstrate that the NOESY distance-constrained backbone torsional conformation was indirectly constrained by the NOE data.

Experimental

DNA Synthesis

The decamer $(CGCTTAAGCG)_2$ was synthesized by a manual modification of the phosphite triester method on a solid support (7, 47, 48). The resulting products were purified by C-18 reverse phase HPLC with an acetonitri1e/triethylammonium acetate (TEAA) gradient on a semi-prep Econosil C18 (Altec) column. The TEAA buffer was a 0.1 M solution at pH 7.2. The sample was detritylated with 80% acetic acid for 25 minutes at room temperature followed by extraction with ether. The sample was desalted by dialysis in a cellulose 1000 molecular weight cut-off dialysis tubing against double-distilled water. After lyophilization, the sample was run through a 1 cm Dowex ion-exchange resin to remove the remaining acetate. The resin had been previously exchanged with KCI. The decamer sample was then treated for one hour with Chelex-100, 200–400 mesh, with repeated vortexing. The decamer was synthesized on a 10 μmole scale. The NMR sample (ca. 10 mg) was dissolved in 100mM phosphate buffer pH 7.0, 100 mM KCl, 1 mM EDTA, and 1 mM sodium azide in a total volume of 600 μl of 99.996% D_2O.

NMR

The ^{31}P one-dimensional NMR experiments, ^{31}P melting curves, the two-dimensional ^{31}P-^{1}H heteronuclear correlation experiments and the two-dimensional ^{31}P J-correlation experiments were acquired on a Varian XL-200 200 MHz spectrometer. The proton one-dimensional spectra, the two-dimensional pure absorption phase NOESY spectra, and the two-dimensional double-quantum filtered COSY (DQF-COSY) spectra were acquired on a Varian VXR-500 500 MHz spectrometer. The proton spectra were referenced to H_2O at 4.80 ppm. The ^{31}P spectra were referenced to trimethylphosphate at 0.000 ppm.

The ^{1}H one-dimensional spectra of the decamer sample were acquired with a sweep width of 8000 Hz and 16K data points. A 90° pulse width of 5.5 μsec and a relaxation delay of 3.0 s were used. The data was processed with a line broadening of 0.5 Hz.

The ^{31}P one-dimensional spectra of the decamer were obtained with a sweep-width of 800 Hz and 1600 data points. A 90° pulse width of 7.8 μs and a total recycle time of 2 s were used. The data was processed with 8K zero filling and a Gaussian apodization function to generate resolution enhancement.

2D NMR Spectra

The two-dimensional pure absorption phase (49) NOESY spectra of the decamer were. acquired at two mixing times: 400 ms and 150 ms. The 400 ms mixing time NOESY spectrum was collected for the assignment of the proton NMR. The 150 ms pure absorption phase NOESY spectrum was acquired to measure the volumes of the proton-proton NOE cross-peaks and thus to measure intra/inter nucleotide distances. The 400 ms NOESY was acquired with a sweep-width of 4498.1 Hz in both the t1 and t2 dimension. The spectrum was collected as 512 FIDs (t1) by 1984 data points (t2). A 90° pulse width of 14.5 μs and a relaxation delay of 2.5 s was used. Sixteen transients were collected for each of the 512 FIDs. The experiment was processed with 2K of zero-filling in the t2 dimension and 1K of zero-filling in the t1 dimension. A Gaussian apodization function was applied in both the

t1 and t2 dimensions to generate resolution enhancement. The spectra were collected with the sample nonspinning. The HDO solvent signal was saturated with the decoupler and a homospoil pulse during the t1 period of the pulse sequence. The 150 ms NOESY experiment was acquired with a sweep width of 5998.8 Hz in both the t1 and the t2 dimension. The spectrum was collected as 256 FIDs (t1) by 2K data points (t2). A 90° pulse width of 23.5 μs and a relaxation delay of 4.5 s was used. Eighty transients were collected for each of the FIDs. The data was processed with 2K of zero-filling in both the t1 and the t2 dimension. A skewed sine-bell apodization function was used in both the t1 and t2 dimension. The apodization function was designed to simply eliminate FID truncation errors without decreasing the intensity of the first data point and without any resolution enhancement. A polynomial baseline correction was applied in both the t1 and t2 dimension.

DQF-COSY

This spectrum was acquired to assign the H5-H6 cytosine protons through their COSY coupling crosspeaks (50). The DQF-COSY spectrum was measured with a sweep-width of 4672.5 Hz in both the t1 and t2 dimension. The spectrum was collected with 1024 FIDs by 4032 data points. Eight transients were collected for each of the FIDs. A 90° pulse width of 12 μs and a relaxation delay of 2s was used. The spectra was collected with the sample nonspinning. The spectra were processed with a zero-filling of 4K in the t1 dimension and 2K in the t2 dimension. A skewed sine-bell apodization function was applied in both the t1 and t2 dimensions to generate resolution enhancement.

$^{31}P/^{1}H$ Pure Absorption Phase Constant Time (PAC)

A version (31, 32) of the Kessler-Griesinger Long-Range Heteronuclear Correlation (COLOC) experiment (51) was conducted on the decamer. The PAC spectra were acquired with a sweep width of 122.8 Hz in the t2 dimension and 641.9 Hz in the t1 dimension. The spectra were collected with 128 transients for each of the 64 FIDs with 256 data points of resolution. A 90° pulse of 7.8 μs for phosphorus and 80 μs for protons was used. The preacquisition delay was 2 s, the constant delay (CD) was 0.051 s and the refocusing delay (RD) was 0.035s. A first order phase correction of 12,075° was used in the O1 dimension. The data was processed with 1K zero filling in the t1 dimension and 512 zero-filling in the t2 dimension. A Gaussian apodization function was applied in both the t1 and the t2 dimension to give resolution enhancement.

Bax-Freeman Selective 2D-J Resolved Long-Range Correlation

This experiment with a DANTE sequence for the selective 180° pulse (52) was conducted on the decamer to correlate the ^{31}P chemical shift with the phosphorus-H3′ coupling constant. The selective 2D-J long-range correlation experiment was acquired with a sweep width of 50 Hz in the t1 dimension and 503.6 Hz in the t2 dimension. A 90° phosphorus pulse width of 7.8 μs, an 8.4 μs proton pulse width and a recycle delay of 1.5 s was used. The DANTE pulse chain consisted of 20 pulses of an approximate length of 9° (total of 180°). In addition, the pulses were separated by a delay of 20 μs. The data set was collected with 355 transients for each of the 32 FIDs (t1) by448 data points (t2). The data was processed with 1K zero-filling in both the t1 and t2 dimension with a Gaussian apodization

plus a negative exponential function to give resolution enhancement in both dimensions. The 2D-J spectra were acquired at 18.5, 30, 50, and 80°C.

The observed three-bond coupling constants were analyzed with a proton-phosphorus Karplus relationship to measure the H3′-C3′-O-P torsional angle θ from which we have calculated the C4′-C3′-O-P torsional angle ε (= –θ – 120°). The relationship, $J = 15.3\cos^2(\theta) - 6.1\cos(\theta) + 1.6$ was determined by Lankhorst et al. (53).

NOESY Distance Restrained Molecular Mechanics/Dynamics Calculations of the Duplex

The initial cartesian coordinates of the decamer were generated using the NUCGEN module of AMBER3 (54) using Arnott right-handed B-DNA coordinates. The program MIDAS (55) operating on a Silicon Graphics Iris 3030 workstation was used for molecular modeling of the decamer. The standard AMBER3 force-field parameters were used. NOESY distance constraints were incorporated into the potential energy force field through addition of a flatwell potential (3, 56; see Results). The different model built structures with 138 NOESY distance constraints from the 150 ms NOESY spectrum were then energy refined until a rms gradient of 0.1 kcal/mol-Å was achieved or until the change in energy was less than 1.0×10^{-7} kcal/mol for successive steps. The energy minimization used the flatwell distance constraints potential with an initial force constant of 10 kcal/mol-Å^2 with a permitted distance error of ±15%. At various stages of refinement, the force constant was increased to a final value of 40 kcal/mol and the permitted error decreased to a final value of ±2.5%. A residue-based cut-off and a distance dependent dielectric function were used. The latter approximates a solution dielectric constant for a gas phase minimization. An 8.5 Å distance cut-off was used for nonbonded pairs interactions. The 1–4 van der Waals and the 1–4 electrostatic interactions had a scale factor of 2.0. A full conjugate gradient minimization was calculated with an initial step length of 5×10^{-4} and a maximum step length of 1.0. The shake routine was not used.

Refinement utilized separate 5 ps cycles of AMBER3 molecular dynamics using the modified potential function which included the NOESY-distance restraining flatwell potential. A Maxwellian distribution was used to calculate the initial velocities at 10 K. The time step for the integration was set to 1 fs, and coordinates were stored every 50 steps. The cutoff distance for nonbonded pairs was set to 8.5 Å, and a distance-dependent dielectric was used. The calculation was done at a temperature of 298.5 K. The calculations used velocity scaling and constant temperature. The 1–4 van der Waals and 1–4 electrostatics were scaled by a factor of 2.0. The charges on the 3′ and 5′ protons were modified to prevent unwanted bond formation. Again, the shake routine was not invoked. All energy minimization and restrained molecular dynamics calculations were carried out on MicroVax II and III computers.

Hybrid Matrix/MORASS Refinement of Structures

A relaxation matrix program (*MORASS: Multiple Overhauser Relaxation Analysis and Simulation*) (46, 57; the program is available upon request) was used to calculate volume and rate matrices as well as implement the hybrid matrix methodology. The well-resolved and measurable crosspeaks in the NOESY spectrum replace the corresponding crosspeaks in the calculated volume matrix, while overlapping or weak crosspeaks and diagonals are

from the calculated spectrum. This hybrid volume matrix, V^{hyb}, is then used to evaluate the rate matrix, whose off-diagonal elements include the effects of spin diffusion. Distances derived from this hybrid relaxation rate matrix (we assume a single isotropic correlation time of 4.0 ns) are then utilized as distance constraints in a 5 ps restrained molecular dynamics simulation. Energy minimization of the averaged last 3 ps structures derived from molecular dynamics completes one cycle of refinement. This process is repeated until a satisfactory agreement between the calculated and observed crosspeak volumes is obtained. As shown by our laboratory (3, 20) and Kaptein and coworkers (26, 27), 3–8 iterations appear to be adequate to achieve convergence to a "refined" structure. This iterative scheme is represented in figure 1.

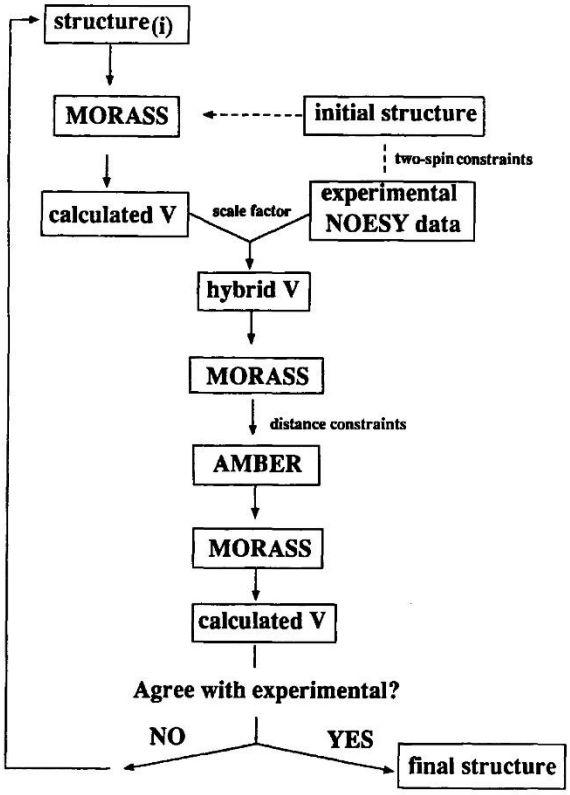

Figure l. Schematic description of the hybrid relaxation matrix method. A hybrid volume matrix V_{hyb} is created by replacing the theoretical volume matrix elements V_{the} with the well-resolved experimental volume matrix elements V_{exp}. The relaxation matrix program MORASS is used to calculate the hybrid (σ/ϱ) rate matrix from the hybrid volume matrix (V_{hyb}). Distances from the rate matrix are then used in a restrained molecular dynamics refinement (AMBER) to yield a new set of coordinates which are used to calculate new theoretical volume and rate matrices. Iteration continues until the experimental and theoretical NOESY volume matrices converge.

Convergence is monitored using equations 1 and 2. The latter criterion is analogous to that used in X-ray crystallography.

$$\%\mathrm{RMS}_{vol} = \sqrt{\frac{1}{N}\sum_{ij}\left(\frac{v_{ij}^{c} - v^{exp}_{ij}}{v_{ij}^{c}}\right)^2} \times 100\% \qquad [1]$$

$$\text{R factor} = \frac{\sum_{ij} | v^{exp}_{ij} - v^{c}_{ij} |}{\sum_{ij} v^{exp}_{ij}} \qquad [2]$$

Convergence is achieved when the $\%\mathrm{RMS}_{vol}$ is within the reliability of the experimental volume measurement. Because most structurally important distances are those from longer-range NOEs, and because these small off-diagonal volumes (< 2% of the diagonal volumes) are the most sensitive to experimental noise, we feel an acceptable RMS error is 20–60% with an R factor of comparable size.

Structure Analysis

The local helical twist was calculated using the AMBER3 analysis module. The structural RMS calculations were determined using an RMS utility program written by Julian Tirado-Rives. The ε and ζ torsional angles and the C4′-C4′ inter-residue distances for the final structure were measured using the GECON program written by Julian Tirado-Rives. The average dihedral angles for the 45 ps dynamics AMBER/MORASS protocol were calculated using the dynamics analysis module MDANAL. The MDANAL module was also used to calculate the time dependency of the six backbone torsional angles and the average C4′-C4′ inter-residue distances.

Results

^{1}H NMR Assignments of the Decamer

The proton spectrum of the decamer sequence $(CGCTTAAGCG)_2$ was assigned through analysis of two-dimensional COSY and NOESY spectra (fig. 2A) via a sequential assignment methodology(5–7, 12, 13). Three H6/H5 COSY crosspeaks were observed in the DQF-COSY spectrum (spectrum not shown) corresponding to the three cytosine bases in the decamer sequence.

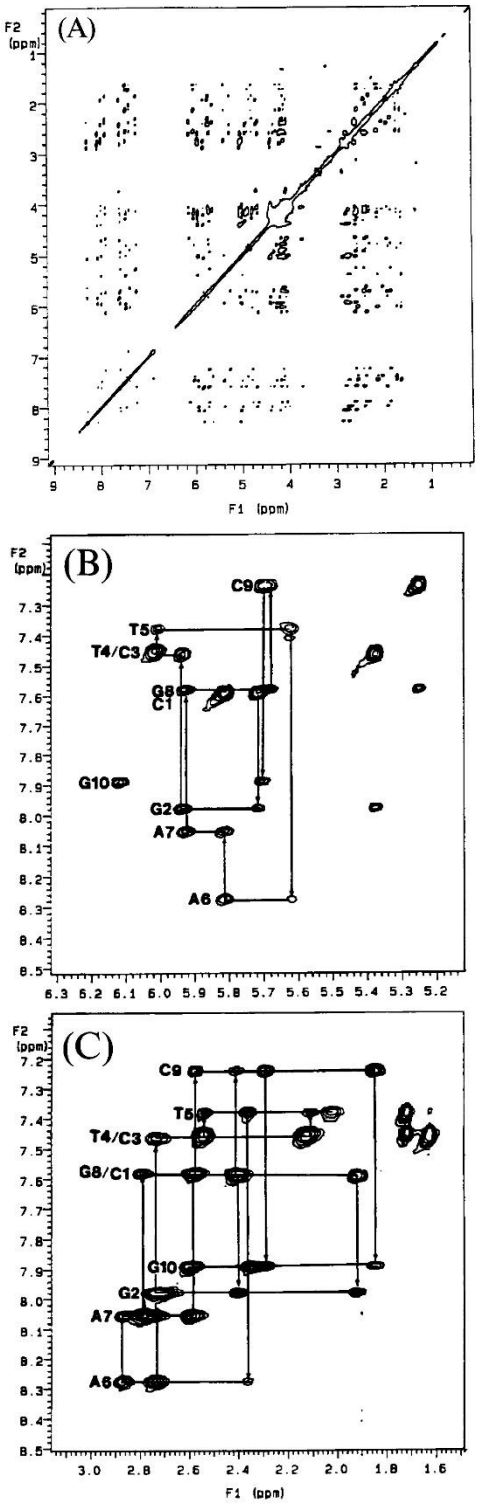

Figure 2. (A) Pure absorption phase 400 ms $^1H/^1H$ NOESY NMR spectrum of duplex decamer, at 500 MHz. (B) The base H8/H6 to H1′ expanded region. (C) Base H8/H6 and deoxyribose H2′,H2″ region. The sequential connectivity of the base H8/H6 and deoxyribose H1′ is diagrammed.

The sequential assignment of the decamer utilized the base-H1′ expanded region of the 2D NOESY spectrum, figure 2B. The assignments proceeded normally except for some ambiguity in the assignment from T4 to C1 because of the degeneracy of the H6 and H1′ resonances of T4 and a cytosine. The degeneracy was confirmed by the H6/H5 cytosine COSY and the thymidine H6-methyl NOE for this H6 resonance. In addition, the H8 resonance of the remaining guanosine (G2) contains three NOE crosspeaks which line up equally well with the NOE crosspeaks of the two remaining cytosines. Based only upon the G2 connectivity, the assignment of C3 and C1 could easily be interchanged. However, the C3 and C1 resonances were differentiated based upon the lack of a clear connectivity to a cytosine from T4. The assignment of C3 to the cytosine degenerate with T4 was consistent with this observation. IfC3 and C1 were reversed, then the connectivity between T4 and C3 would have to be assumed missing instead of being a degenerate peak.

Other features of the spectrum confirm the assignments of C3 and C1. The T4 H6 to its own H1′ NOE was very large and broad. It was reasonable to assign this peak as a degenerate NOE containing, in addition to the T4 H6 to its own H1′ NOE, the T4 H6 to C3 H1′ NOE and the C3 H6 to its own H1′ NOE. Both G8 and G2 contain an additional NOE crosspeak. For G8, this additional crosspeak occurred between the G8 H8 proton and the C9 H5 proton. The additional G2 crosspeak would correspond to a NOE between the G2 H8 proton and the C3 H5 proton with the current assignments of C3 and C1. This was consistent with the 5′ directionality expected and exhibited by G8. Based upon these observations, the assignment continued from theT4/C3 degenerate crosspeak to the C3 H6(7.48 ppm) to G2 H1′ (5.94ppm) NOE. This NOE showed a connectivity to the G2 H8 (7.99 ppm) to its own H1′ NOE which connected with the G2 H8 to C1 H1′ (5.74ppm) NOE. The G2 H8 to C1 H1′ NOE had a connectivity to the C1 H6 (7.62 ppm) to its own H1′ NOE. This showed a connectivity to the C1 H6 to H5 (5.86ppm) NOE and as expected for the 5′ end base the NOE between the base proton and the 5′ end H1′ sugar proton did not exist.

The expanded region of the 400 ms NOESY spectrum corresponding to the H8/H6 base region contained numerous NOEs (spectrum not shown, all spectra not shown may be obtained from the authors). These base-base crosspeaks arise from spin-diffusion and occur between neighboring bases. The three guanosine and the two adenosine base resonances gave NOEs to either the 5′ base, the 3′ base, or both the 5′ and 3′ base.

The expanded region of the 2D NOESY experiment corresponding to the H8/H6 to H2′/H2″ region provided confirmation of the sequential assignment of the decamer (fig. 2C). Remarkably, the same problem with the degenerate thymidine and cytosine resonances occurred in the H8/H6 to H2′/H2″ region. The H8/H6 to H2′/H2″ region indicated that the T4 and C3 H2′/H2″ protons were also degenerate since only four NOE peaks were observed. This was also confirmed by the HI′ to H2′/H2″ region. The H8/H6 to H1′ region established that the T4 and C3 Hl′ protons were degenerate. The Hl′ proton corresponding to this chemical shift (6.01 ppm) contained only two NOE crosspeaks corresponding to chemical shifts of 2.55 and 2.13 ppm for the H2″ and the H2′ protons of T4 and C3.

The degenerate T4/C3 H6 peak contained two NOEs to methyl protons. One NOE corresponded to the T4 H6 to T5 methyl, the other corresponded to the T4 H6 to methyl (1.64 ppm) NOE. The existence of these NOE crosspeaks to methyl protons confirms the degenerate T4/C3 H6 assignment.

The H2′ and H2″ resonances were stereospecifically assigned by the relative magnitude of the NOE between the H1′ proton and the H2′ and H2″ protons. In B-DNA, the distance between H1′ and H2′ is longer than the H1′ to H2″ distance. The NOE with the smallest volume corresponds to the H2′ proton. Also, the chemical shift of H2′ is generally upfield from the H2″ proton, but the assignment was based strictly on the integrated NOE volumes.

The additional sugar protons, H3′, H4′, and H5′/H5″ were assigned from the NOE crosspeaks to H1′ and H8/H6 protons (spectra not shown). The H3′, H4′, and H5′/H5″ protons were distinguished by their relative chemical shifts. The H3′ protons are further downfield from the H4′ protons which are further downfield from the H5′/H5″ protons. The H5′ and H5″ protons resonances were not stereospecifically assigned.

The nearly complete assignment of the decamer's ^{1}H NMR spectrum is listed in table I. The chemical shifts of all the common C3 and T4 protons were degenerate. The assignments of the decamer's ^{1}H NMR spectrum allowed for the measurement of NOE volumes using VNMR and calculation of the corresponding interproton distances.

Table I. Non-Exchangeable Proton Chemical Shifts (ppm) of d(CGCTTAAGCG)

				PAC(a,b)/Noesy(a,c)				
BASE	H6/H8	H5	H1′	H2′/H2″	H3′	H4′	H5′/H5″	CH3
C1	7.62	5.86	5.74	1.94/2.41	4.70/4.69	—	4.08/3.73	—
G2	7.99	—	5.94	2.59/2.76	4.99/4.98	4.41	4.10/4.01	—
C3	7.48	5.39	5.74	2.13/2.55	/4.86	4.26	4.17/4.15	—
T4	7.45	—	5.74	2.13/2.55	/4.86	4.26	4.17/4.15	1.64
T5	7.38	—	5.62	2.02/2.36	4.87/4.87		4.11/4.11	1.72
A6	8.27	—	5.82	2.73/2.86	5.05/5.04	—	4.11/4.11	—
A7	8.05	—	5.92	2.59/2.76	5.02/5.02	4.43	4.20/4.20	—
G8	7.58	—	5.69	2.41/2.57	4.89/4.91	4.39	4.17/4.17	—
C9	7.24	5.26	5.71	1.85/2.29	4.92/4.91	4.39	4.13/4.13	—
G10	7.90	—	6.12	2.59/2.36	/4.66	4.15	4.16/4.05	—

(a) Proton chemical shifts referenced to HDO at 4.76 ppm.

(b) Chemical shifts assigned from the P-31/H-1 2D PAC spectrum.

(c) Chemical shifts assigned from the H-1/H-1 NOESY spectrum.

^{31}P Resonance Assignments of the Decamer

The assignment of the resonances in the ^{31}P spectrum of the decamer (fig. 3) is based upon a *P*ure *A*bsorption phase, *C*onstant time $^{1}H/^{31}P$ heteronuclear correlated spectrum, PAC (31) (fig. 4). The PAC experiment contains crosspeaks between the phosphorus resonance and the H3′, H4′, and H5′/H5″ protons via long-range coupling. Thus, with the known H3′ chemical shift assignments from the 2D-NOESY spectrum the corresponding phosphorus resonances were assigned (fig. 3). Seven of the nine resonances were assigned by this technique. Because of the degeneracy of the H3′ protons of the C3 and T4 residues, the phosphorus resonances of C3 and T4 have been tentatively assigned based upon the PAC crosspeak between the H5′ proton of T5 and the T4 phosphate. The decamer phosphorus

assignments with the corresponding $J_{H3'-P}$ coupling constants at various temperatures are listed in table II.

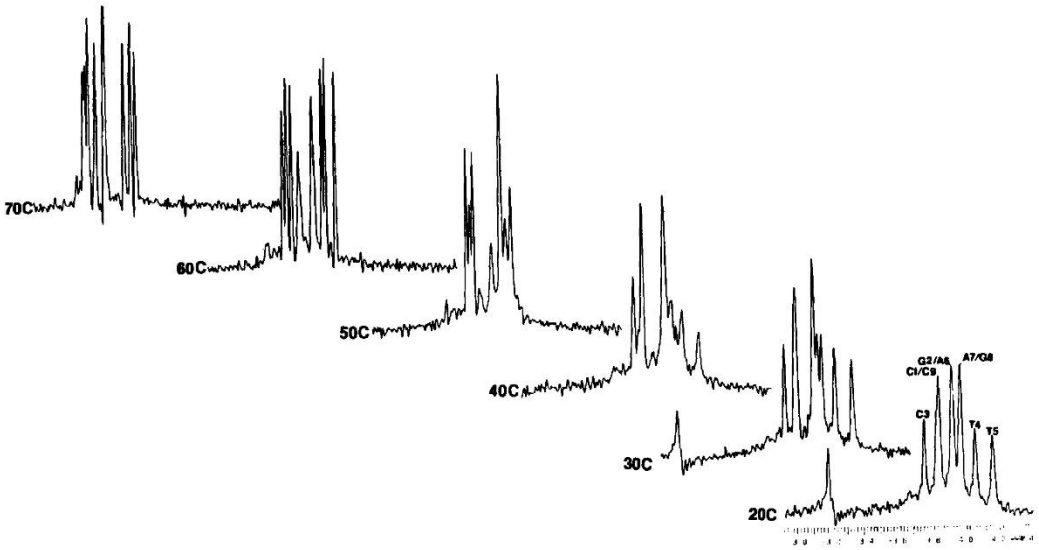

Figure 3. ^{31}P NMR spectra and phosphate assignments of decamer (numbering corresponds to phosphate position from the 5′-end of the duplex) at indicated temperatures.

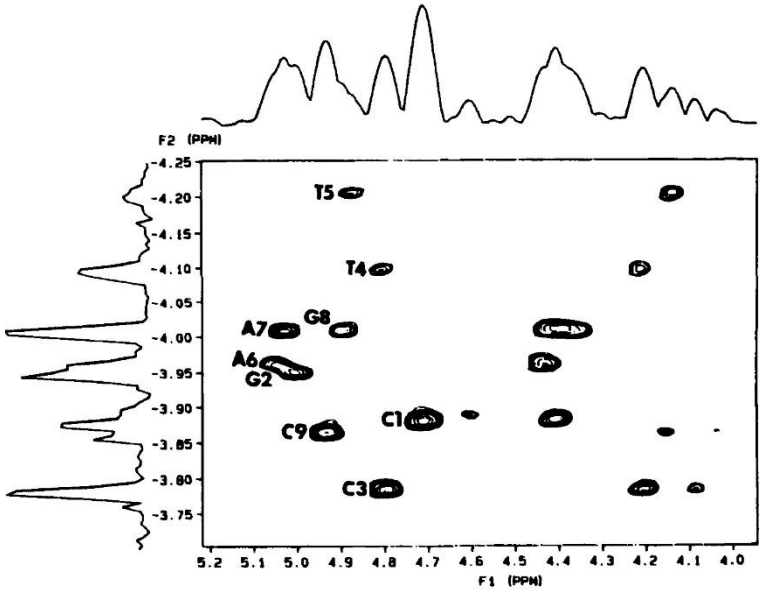

Figure 4. Two-dimensional ^{31}P-^{1}H PAC heteronuclear correlation NMR spectrum of duplex decamer at 200 MHz (^{1}H). The 1D decoupled ^{31}P NMR spectrum is shown along one axis and the H3′, H4′, and H5′,H5″ region of the proton spectrum is shown along the second axis.

Table II. ^{31}P Chemical Shifts (ppm) and J(P-H3′) (Hz) Coupling Constants for Decamer at Indicated Temperatures

BASE	^{31}P (ppm)	18.5°C J(P-H3′) Hz	30°C J(P-H3′) Hz	50°C J(P-H3′) Hz	80°C J(P-H3′) Hz
C1					
p	–3.884	4.1	4.6	5.6	6.2
G2					
p	–3.952	< 2	2.6	3.6 or 6.2	5.4 or 6.6
C3					
p	–3.791	5.5	5.0	5.6	6.8
T4					
p	–4.103	2.7	3.4	3.8	6.0
T5					
p	–4.207	2.7	2.8	4.0	6.4
A6					
p	–3.965	< 2	2.6	3.6 or 6.2	5.4 or 6.6
A7					
p	–4.012	< 2 or 3.0	3.4	3.6 or 6.2	5.4 or 6.6
G8					
p	–4.012	< 2 or 3.0	3.4	3.6 or 6.2	5.4 or 6.6
C9					
p	–3.865	4.1	4.6	5.6	6.2
G10					

^{31}P Melting Curve

The temperature dependence of the ^{31}P chemical shifts is shown in figure 5. As expected, (29, 37) the main cluster of resonances moves downfield with increasing temperature. Above 50°C, the decamer is expected to be in a completely single-stranded form.

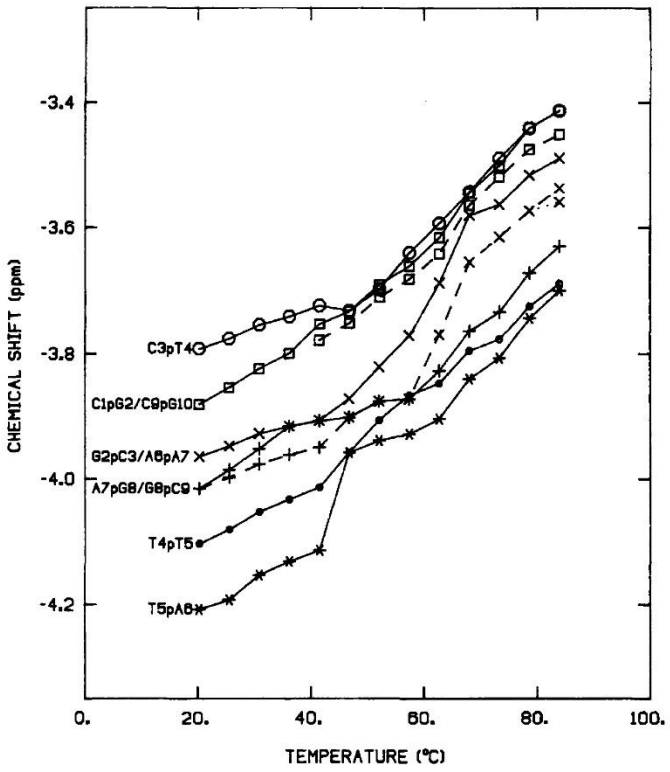

Figure 5. Temperature dependence of ^{31}P chemical shifts of duplex decamer.

J-Resolved Spectra

The $J_{H3'-P}$ coupling constants were measured with the 2D-J resolved long-range correlation spectrum (fig. 6). Table II lists the $J_{H3'-P}$ coupling constants. We have utilized these coupling constants and a proton-phosphorus Karplus relationship (see Experimental Section) to determine the H3′-C3′-O-P torsional angle θ from which we have calculated the C4′-C3′-O-P torsional angle ε. Up to four different torsional angles (0–360°) may be derived from the same coupling constant. We assume that the torsional angle closest to the crystallographically observed ε = –169 ± 25° (58) is the correct value. As shown by Dickerson (41, 59) there is a strong correlation (R = –0.92) between torsional angles ζ and ε in the crystal structures of a dodecamer (ζ may be calculated from the relationship (41, 59)ζ = –317–1.23ε). Assuming this correlation of ζ and ε exists for other duplex structures in solution as well, and from the measured coupling constants, we can calculate both C4′-C3′-O3′-P (ε) and C3′-O3′-P-O5′ (ζ) torsional angles. A comparison of the variation of both the coupling constants (as well as ζ and ε) and ^{31}P chemical shifts for the decamer sequence is shown in figure 7.

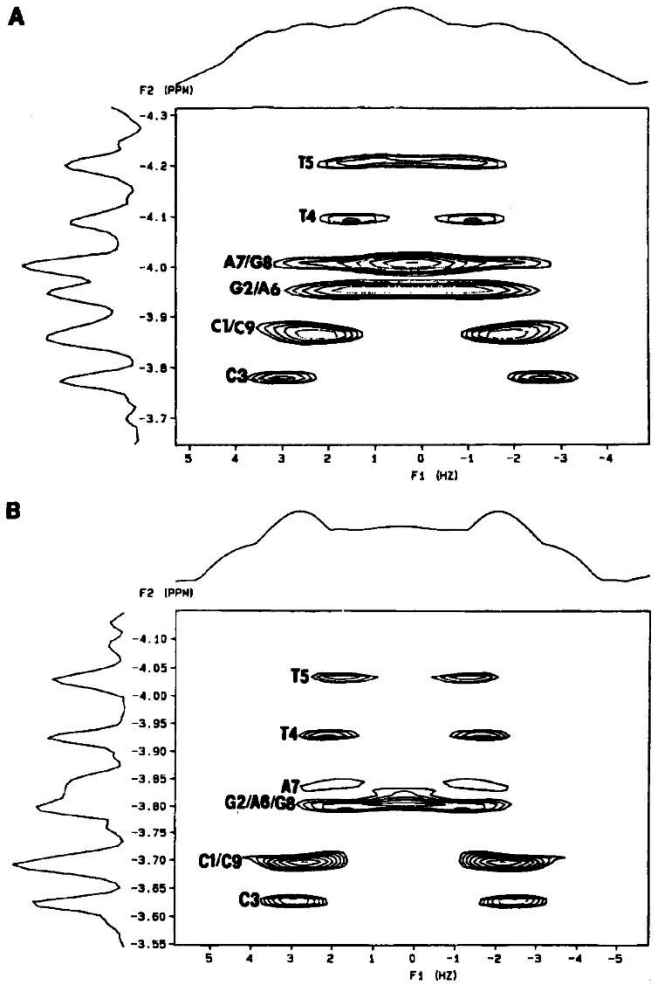

Figure 6. 2D-J resolved $^{31}P/^{1}H$ spectrum of the decamer. The 1D decoupled ^{31}P NMR spectrum is also shown along one axis, and the H3′ coupled doublets are shown along the second dimension. (A) 18.5°, (B) 30°, (C) 50°, (D) 80°.

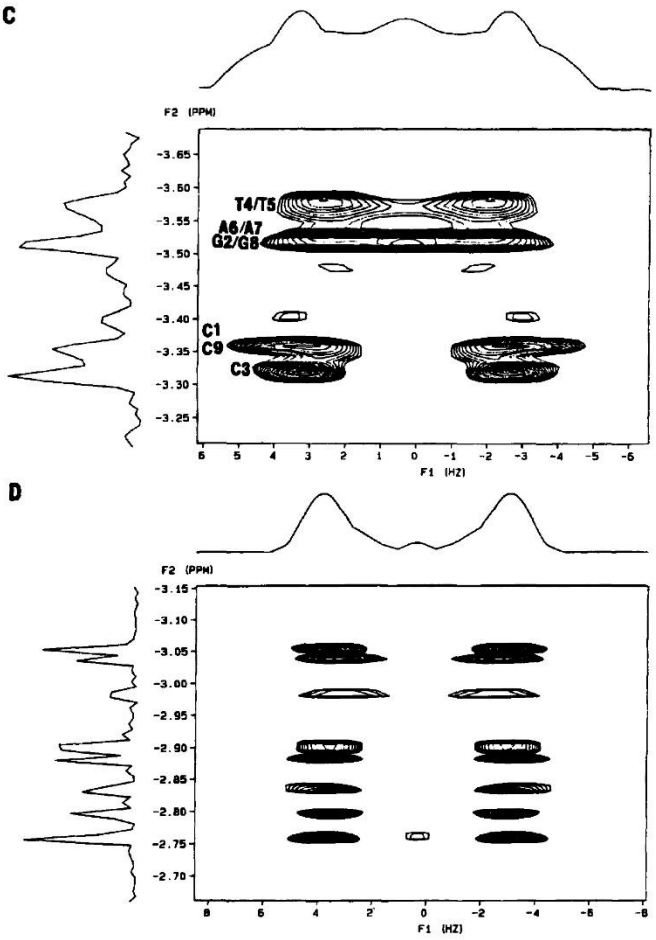

Figure 6, *continued*

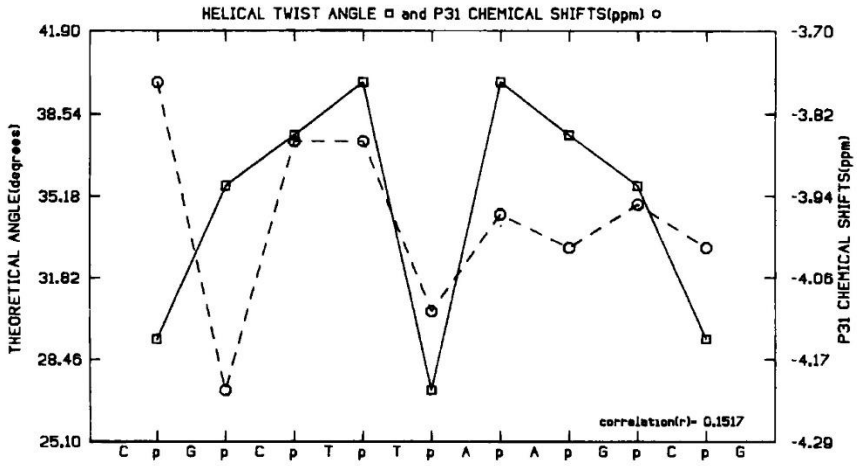

Figure 7. Plot of ^{31}P chemical shifts (--o--) for the decamer vs. phosphate position along the 5′-3′ strand. Also shown is a plot of calculated helix twist, t_g, derived from calculated Σ_1 sum function and equation 1($t_g = 35.6 + 2.1\Sigma_1$) vs. phosphate position (—□—). The t_g vs. sequence plot has been scaled to reflect the ^{31}P chemical shift variations.

The correlation coefficient between the coupling constants and ^{31}P chemical shifts varies from 0.92 (at ambient temperature) to 0.89 (at 50°C) and even 0.55 at 80°C. Similar correlation between $J_{H3'-P}$ coupling constants and ^{31}P chemical shifts has been observed for all other oligonucleotide duplexes (36, 45).

Discussion

NMR Structural Refinement from 2D NOESY Distances

Evaluation of interproton distances from a 2D-NMR NOESY spectrum has generally relied on the so-called "two-spin approximation" (17, 21). The approximation requires that the NOESY derived distances be obtained from vanishingly short experimental mixing times where the rate of build-up of the NOE crosspeak intensity is ca. linear and the effects of spin diffusion are minimal. Because most of the structurally important longer range NOEs are not observed at these short mixing times, the use of the two-spin approximation has raised concern over the validity of refined NMR structures derived by this methodology (3, 20, 22). The effects of spin diffusion increase with an increase in mixing times and at a mixing time of 150 ms can introduce significant errors in measured distances (3, 20, 22, 46). The two-spin approximation suffers from low sensitivity at short mixing times and spin diffusion at longer mixing times. It is obvious that it is inherently difficult to obtain accurate distances from volumes using the two-spin approximation.

Therefore, a hybrid relaxation matrix procedure was employed to correct for multi-spin effects at this longer mixing time. At 150 ms, 138 NOESY constraints (per duplex) were measured (table III).

Table III. Distances (A) measured from NOESY spectra and derived from the final MORASS restrained molecular dynamics structure

Intranucleotide Distances (R_{ij})[a,b]					
Base	H6/H8 to H1′	H6/H8 to H2′/H2″	H1′ to H2′/H2″	H1′ to H3′	H3′ to H2′/H2″
C1	3.11 (3.33)	2.68/— (2.60)	3.04/2.58 (3.94/2.52)	—	2.56/2.95 (2.36/2.74)
G2	3.41 (3.73)	—/2.28 (3.14)	—/—	2.62 (3.28)	—/2.20 (2.65)
C3	—	—/—	—/—	—	—/—
T4	—	—/—	—/—	—	—/—
T5	3.14 (3.18)	2.43/2.78 (2.20/3.39)	2.80/2.39 (3.22/2.34)	3.07 (3.25)	2.58/2.57 (2.23/2.62)
A6	3.65 (4.09)	2.51/2.91 (2.44/3.55)	2.51/2.40 (2.94/2.43)	2.80 (3.03)	2.57/2.63 (2.37/2.70)
A7	3.60 (3.88)	2.55/3.08 (2.40/2.80)	—/—	—	2.47/— (2.32)
G8	3.56 (3.69)	—/—	2.72/2.43 (2.88/2.42)	—	2.64/2.51 (2.34/2.55)
C9	3.07 (3.21)	2.54/3.04 (2.16/3.44)	2.94/2.44 (3.50/2.47)	—	2.70/— (2.36)
G10	3.49 (3.81)	2.46/3.06 (2.31/3.79)	2.68/2.36 (2.89/2.41)	3.42 (4.00)	2.53/2.67 (2.41/2.81)

Intranucleotide Distances (R_{ij-1})[a,b]			
Base	H6/H8 to H1′	H6/H8 to H2′	H6/H8 to H2″
C1	—	—	—
G2	3.97 (5.56)	3.14 (3.19)	3.03 (2.97)
C3	2.97 (3.07)	—	2.71 (2.50)
T4	—	—	—
T5	3.60 (4.20)	3.09 (3.67)	2.74 (2.41)
A6	4.24 (4.82)	3.63 (3.95)	3.35 (3.33)
A7	3.36 (3.47)	—	3.08 (2.80)
G8	3.17 (3.42)	—	2.84 (2.30)
C9	—	2.94 (3.26)	3.25 (2.35)
G10	3.93 (2.95)	3.40 (4.22)	3.07 (2.50)

a. All distances referenced to C3 (H5/H6) crosspeak, assuming a reference distance of 2.45 Å.
b. The final MORASS iteration (B-DNA (I) 9) distances are given underneath the two-spin distances in parenthesis.

Only those crosspeaks that could be adequately resolved from overlapping peaks were included. Note that degeneracy of the C3 and T4 proton resonances prevented the measurement of any intra-residue distances involving these residues, limiting the total number of distance constraints. Detailed structural information about these residues is thus missing. No imino hydrogen bond constraints were added. The typical refinement follows the iterative hybrid matrix/MORASS/restrained molecular dynamics methodology incorporating the NOESY distance constraints as described previously (fig. 1). Initial structures were used to calculate a theoretical NOESY volume matrix which was merged with the experimental NOESY matrix using MORASS. After the volume matrix is calculated, the data sets are scaled by using the resolved cytosine H5-H6 NOEs and H2′-H2″ fixed distance crosspeaks. As many scaling NOEs as possible were used, and an average scaling factor (26) was used. The MORASS calculation requires an approximate correlation time (3, 46). However an advantage of the MORASS scaling methodology is to minimize errors associated with inaccurate estimates of the correlation time. The single isotropic correlation time was estimated based upon related values in the literature (60, 61).

A stepwise or perturbational merging was implemented to improve the diagonalization behavior of the hybrid volume matrix. A set of empirical rules were established to determine the amount the theoretical volumes were incremented towards the experimental volumes. This was determined by the relative difference between the theoretical and experimental volumes. The incremental change in the theoretical volume decreased as the relative volume difference increased. These empirical rules were part of the MERGE module of the MORASS program and were executed automatically. This “gentle nudging” of the intermediate structures avoids dramatic changes in one iteration which can produce an ill-conditioned mathematical problem during the transformation of the incorrect initial structure to the final structure.

The back-calculation of the merged volume matrix yielded a new rate matrix from which a new set of distances is calculated. At this stage the new distances now better account for any spin diffusion. The new distances were then used as constraints in a molecular mechanics calculation followed by a 5 ps restrained molecular dynamics run. The molecular dynamics calculations allows the structure to jump out of local energy minima and move toward the correct solution structure driven by the experimental distances. The 3–5 ps structures from the dynamics run were averaged and then reminimized. The new set of distances from this minimized structure was then used to calculate a new NOESY spectrum which was then compared again with the experimental spectrum. This completed one iteration cycle and continued until no further improvements in the fit of the theoretical spectrum were obtained. Full merging occurred by the 9th iteration. This basic iterative scheme (see fig. 1) was followed until the $\%RMS_{vol}$ (equation 1) converged to a limiting value as outlined in table IV.

Table IV. Calculated Energies for the Decamer during Restrained Molecular Dynamics Structural Refinement Starting from the B-DNA(I) Model

Structure[a]	I[b]	Energy[c]	Constraints[c]	Energy[d]	Constraints[e]	%RMS(exp)[f]	%RMS(the)[f]	R[g]
BDNA		–770	0	–770	0	—	—	—
MIN.		–572	75.6	–883	273.3	—	—	—
DYN.AVG.		–622	63.7	–851	282.9	—	—	—
MORASS	1	–715	13.9	–869	35.4	145.18	412.53	0.4231
MORASS	2	–707	16.6	–856	100.6	125.13	248.24	0.3856
MORASS	3	–733	2.5	–850	60.5	122.41	276.56	0.4199
MORASS	4	–729	1.7	–858	14.1	128.65	77.01	0.3705
MORASS	5	–667	45.7	–878	44.2	114.98	80.57	0.3809
MORASS	6	–546	120.9	–835	53.8	81.61	69.10	0.3434
MORASS	7	–633	52.9	–837	26.4	79.88	79.15	0.3673
MORASS	8	–612	67.4	–842	29.4	84.32	65.08	0.3447
MORASS	9	–631	52.4	–846	26.0	79.84	64.30	0.3478

a. Structure identifiers: B-DNA-Arnott model built structure, MIN-minimization with two spin constraints, DYN. AVG. 3–5 psec dynamics averaged structure with two spin constraints, MORASS-MORASS iteration.

b. MORASS iteration number.

c. The total energy (kcal/mol Å^2) of the structure from the AMBER minimization of the 3–5 psec dynamics averaged structure and the corresponding constraint energy. Constraints for MORASS iterations 1–4 were 20 kcal/mol Å^2 with 15% allowed error in the flatwell distance constraining harmonic term. For iteration 5, 30 kcal/mol Å^2 and a 5% allowed error were used. For iterations 6–9, a 40 kcal/mol Å^2 and a 2.5% allowed error were used.

d. The total energy (kcal/mol Å^2) of the structure minimized without any distance constraints.

e. The constraint energy (kcal/mol Å^2) of the structure minimized with a constraint force constant of 20 kcal/mol Å^2 and an allowed error of 5% in the flatwell distance constraining harmonic term.

f. %RMS difference (equation 1) between the experimental and theoretical volumes relative to either (exp) experimental volumes or (the) theoretical volumes.

g. R-factor (equation 2).

Table IV, *continued*. Calculated Energies for the Decamer during Restrained Molecular Dynamics Structural Refinement Starting from the B-DNA(II) Model

Structure[a]	I[b]	Energy[c]	Constraints[c]	Energy[d]	Constraints[e]	%RMS(exp)[f]	%RMS(the)[f]	R[g]
BDNA		–770	0	–770	0	—	—	—
MIN.		–572	75.6	–883	273.3	—	—	—
DYN.AVG.		–622	63.7	–851	282.9	—	—	—
MORASS	1	–704	15.5	–837	146.1	108.51	299.70	0.3745
MORASS	2	–741	1.6	–857	21.4	111.18	220.42	0.3718
MORASS	3	–750	1.4	–862	32.2	117.21	260.89	0.4066
MORASS	4	–744	1.1	–858	25.9	74.29	144.00	0.3387
MORASS	5	–700	17.6	–839	15.8	83.91	132.95	0.3367
MORASS	6	–580	101.9	–845	51.9	82.94	100.28	0.3232
MORASS	7	–659	36.4	–850	17.1	76.90	89.32	0.3219
MORASS	8	–662	36.7	–844	18.2	65.32	81.43	0.3131
MORASS	9	–654	37.7	–844	17.9	60.35	85.26	0.3111

a. Structure identifiers: B-DNA-Arnott model built structure, MIN-minimization with two spin constraints, DYN. AVG. 3–5 psec dynamics averaged structure with two spin constraints, MORASS-MORASS iteration.

b. MORASS iteration number.

c. The total energy (kcal/mol Å^2) of the structure from the AMBER minimization of the 3–5 psec dynamics averaged structure and the corresponding constraint energy. Constraints for MORASS iterations 1–4 were 20 kcal/mol Å^2 with 15% allowed error in the flatwell distance constraining harmonic term. For iteration 5, 30 kcal/mol Å^2 and a 5% allowed error were used. For iterations 6–9, a 40 kcal/mol Å^2 and a 2.5% allowed error were used.

d. The total energy (kcal/mol Å^2) of the structure minimized without any distance constraints.

e. The constraint energy (kcal/mol Å^2) of the structure minimized with a constraint force constant of 20 kcal/mol Å^2 and an allowed error of 5% in the flatwell distance constraining harmonic term.

f. %RMS difference (equation 1) between the experimental and theoretical volumes relative to either (exp) experimental volumes or (the) theoretical volumes.

g. R-factor (equation 2).

The distance constraining pseudo-force constants were gradually increased from 10 to 40 kcal/mol/Å^2 and the estimated distance error brackets were gradually decreased from ±15 to ±2.5%. The decamer structure was refined from two initial structures corresponding to the molecular mechanics minimized structure of a model-built Arnott B-DNA [B-DNA(I)], and a molecular dynamics (5 ps) averaged structure of a model-built Arnott B-DNA [B-DNA(II)]. Distance constraints (using the two-spin approximation) were incorporated into either of the initial starting structures. The progress of the MORASS/restrained MD refinement for the two initial structures is shown in tables IV/V and lists overall energy, constraint energy, RMS percent volume differences (%RMS$_{vol}$), R factor, and distance RMS. Figure 8 shows the structures after the 9th, 5 ps, merge matrix iteration cycle (total 45 ps MD) starting from both the initial B-DNA(I) and II models. Figure 8 is a comparison of the initial model built structure and the final structures from the MORASS/AMBER protocol.

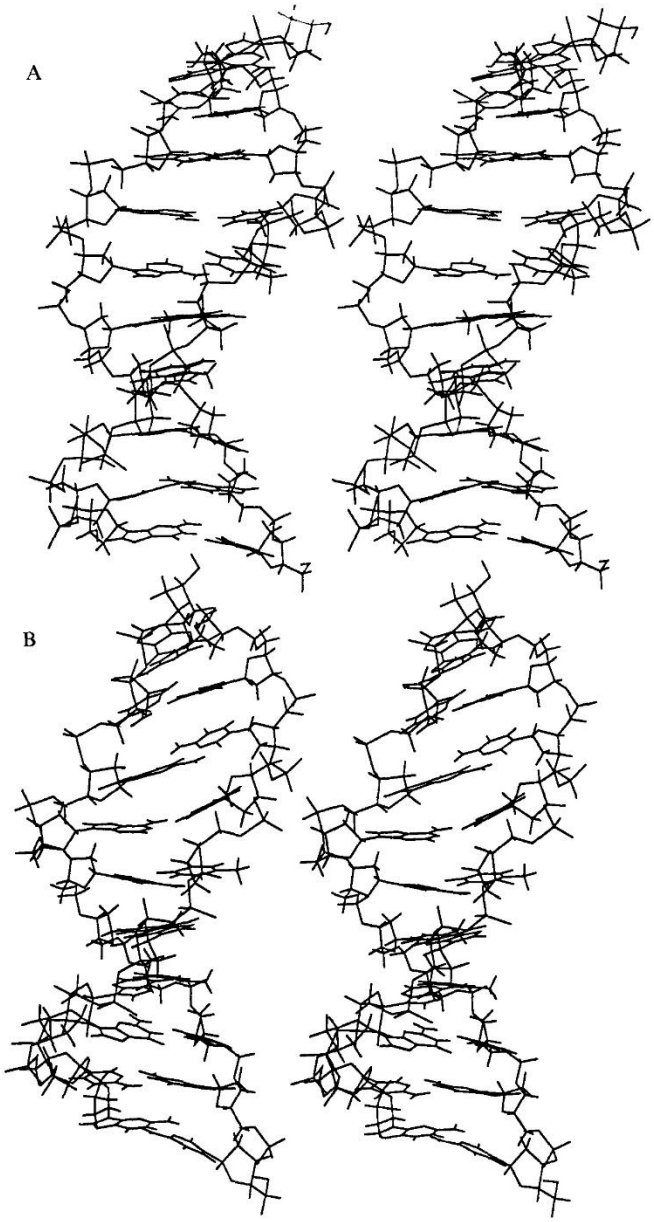

Figure 8. Stereoviews of the final (9th iteration cycle) NOESY-distance restrained, molecular dynamics decamer structures, starting from B-DNA(I) (A) and B-DNA(II) (B) and stereoview overlay of final, 9th iteration cycle structures B-DNA(I) and B-DNA(II) (C).

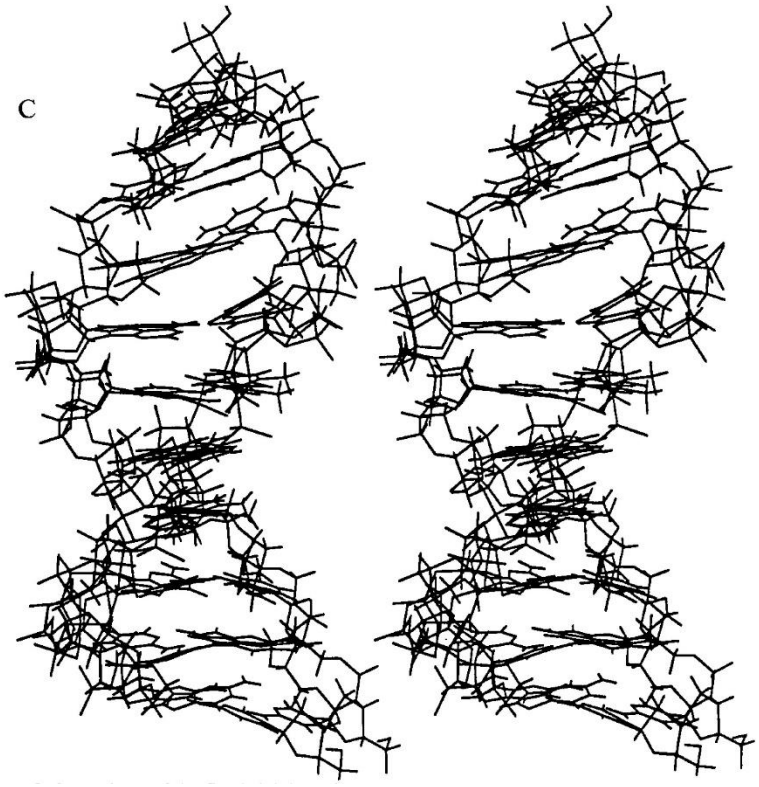

Figure 8, *continued*

The final MORASS refined duplex was the reference structure for the RMS calculations in all cases. The convergence in the MORASS refinement was monitored by the $\%RMS_{vol}$ and R factor. The $\%RMS_{vol}$ were based on equation 1 in which the denominator contained either the theoretical or experimental volumes (table IV). The R factor (equation 2), directly analogous to the R factor used for crystallographic refinement, seemed to be of marginal utility in monitoring convergence. In general there is a slight decrease in the R factor during the refinement cycles (decreasing from approximately 0.4 to 0.3). We believe our $\%RMS_{vol}$ factor better represents the quality of the NMR refinement than the R factor (3, 20, 28, 62). The latter heavily weighs the large NOESY volumes. The absolute errors associated with the large volumes are considerably larger than those of the small volumes and dominate the summation in both the numerator and the denominator in the R factor. These large volumes correspond to short distances, and many of these short distances in DNA represent sugar ^1H-^1H intra-furanose distances which are not very sensitive to the overall geometry of the duplex. The longer distances define the inter-residue constraints and are therefore much more important in refining features of the structure such as the orientation and position of the base-pairs. Our $\%RMS_{vol}$ factor *equally* weighs the small and large volumes by summing the *percentage* errors in these volumes (equally weighing a 20% error in a large and small volume while that of equation 2 would place a much heavier weight on

the error in the large volume). Thus we believe the $\%RMS_{vol}$ factor defined in equation 1 is a more useful criterion for convergence and quality of fit for NMR data.

Progress in the MORASS/restrained MD refinement was also monitored by the change in the overall and the constraint energies (table IV). While the minimized potential energies shown in table IV appear to increase as the refinement progresses, this is entirely attributed to the increased constraint energy term resulting from the increasing constraint force constants and the narrower error limits imposed on the structures. Note though that iterations 1 through 4 used a constant constraining potential function, and the total energy as well as the constraint energies decrease through these iterations. Unconstrained energy minimization of the 5 ps restrained MD structures shows no trend in the energy as the refinement progresses (table IV). The force constants for the distance constraints and the distance error bars were changed after the fourth, fifth, and sixth iteration. These changes initially caused an increase in the total energy and constraint energy relative to the previous iterations. Initially, the constraints were chosen to be relatively modest because during the early refinement cycles the distances are still quite inaccurate. As the refinement progresses, spin diffusion is better taken into account and the constraining potential error limits are reduced. In the final iterations, the choice of the distance constraint potential function was not important.

Using a constant flatwell constraint penalty function (%error = 5%; harmonic force constant, k = 20 kcal/mol/Å^2), the constraint energy decreases from ca. 280 kcal/mol to ca. 17–26 kcal/mol during the merge matrix refinement steps, table IV. However, because the equilibrium constraint distances are also changing with each iteration, comparison of constraint energies and distance violations may be misleading.

The best indicator of convergence was provided by the $\%RMS_{vol}$ (theoretical volumes) which decreased from values on the order of 300–400% to 60–80%. Overall, after 9 iterations the theoretical and experimental volumes have converged for both the BDNA(I) and B-DNA(II) starting structures. The process also indicates the presence of two poorly defined distances. The bad NOE crosspeaks correspond to the G4 H8-H2″ and G4 H3′-H2″ intraresidue NOEs. Iterative refinement did not improve the fit of the calculated crosspeak volumes relative to the experimental volumes. This indicated that the structure was unable to accommodate these two volumes, implying an error in the measured volumes.

A possible problem in the MORASS calculation was the choice of a correlation time. In the decamer we estimated a correlation time of 4.0 ns. This value gave a best fit to the theoretical NOESY build-up curves for the final refined structure (curves not shown). Further, we have shown (20) that with proper scaling of the experimental and theoretically calculated volumes, an incorrect estimate of τ_c has negligible effects on the derived distances. Changes in the calculated volumes become significant only at large changes in correlation times (>1 ns). We are therefore confident that although our method is in part dependent on a reasonably correct τ_c estimate, much of the potential error possibly introduced by the choice of a poor τ_c is corrected for by scaling of the data sets. Thus, problems arise only if the estimate of the correlation time is significantly in error (20, 46).

Separate refinement paths from both B-DNA(I) and B-DNA(II) appear to converge to a similar final structure (figure 8) with similar $\%RMS_{vol}$ and distance constraint violations. The RMS differences between the cartesian coordinates derived from the final structures

[B-DNA(I) 9th iteration and B-DNA(II) 9th iteration] are compared in table VA/B). The final 1.4 Å RMS difference between the set of constrained distances in the B-DNA(I) 9th iteration and B-DNA(II) 9th iteration structures is comparable to the RMS distances between any two sets of refined structures (for example the RMS deviation of distances between B-DNA(I) 8th/iteration and BDNA(I) 9th iteration structures are 1.3 Å. Each of these latter refinement cycle structures are thus equally valid and refinement can only be defined in terms of a family of comparable structures. Figure 8C depicts the overlay of the final, 9th iteration, structures B-DNA(I) and B-DNA(II). Although local differences in the structures may be small, their cumulative effect over the length of the helix can be quite large. Thus while the short-range distances are well defined it is very difficult, if not impossible, by NMR to define long-range structural differences when only short-range distances are used as constraints.

Table V. RMS Difference (Å) of the Constraining Distances for the Decamer during Restrained Molecular Dynamics Structural Refinement Starting from the B-DNA (I) Model (A) or the B-DNA (II) Model (B)

(A) B-DNA I				(B) B-DNA II			
Structure[a]	I[b]	RMS(Å)[c]	RMS(Å)[d]	Structure[a]	I[b]	RMS(Å)[d]	RMS(Å)[c]
BDNA		1.9964	1.7741	BDNA		1.7741	1.9964
MIN.		1.9835	1.7735	MIN.		1.7735	1.9835
DYN.AVG.		2.2551	1.9507	DYN.AVG		1.9507	2.2551
MORASS	1	2.1139	1.7360	MORASS	1	2.0295	2.3801
MORASS	2	2.2400	1.7660	MORASS	2	1.6278	2.0770
MORASS	3	2.1102	1.9781	MORASS	3	1.6164	2.1585
MORASS	4	2.1168	1.9781	MORASS	4	1.6765	1.9382
MORASS	5	1.7387	1.9818	MORASS	5	1.8380	2.2865
MORASS	6	1.7895	1.1909	MORASS	6	1.0342	1.7657
MORASS	7	0.9486	1.3239	MORASS	7	1.3239	1.5414
MORASS	8	1.3000	1.0136	MORASS	8	0.8657	1.5162
MORASS	9	0.0000	1.4136	MORASS	9	0.0000	1.4136

a. Structure identifiers: B-DNA-Arnott model built structure, MIN-minimization with two spin constraints, DYN. AVG. 3–5 psec dynamics averaged structure with two spin constraints, MORASS-MORASS iteration.

b. MORASS iteration number.

c. Final B-DNA I structure is the RMS reference structure.

d. Final B-DNA II structure is the RMS reference structure.

Structural Analysis

Analysis of the local helical parameters derived from the hybrid matrix/MORASS/restrained MD refined structure for the decamer provides support for the validity of the derived structures. The decamer's helical twist, dihedral torsion angles, and the C4′-C4′ interresidue distances were calculated for the final structure and averaged over the 45 ps of dynamics for the entire refinement procedure for the B-DNA(I) model.

Local helical distortions arise along the DNA chain due to purine-purine steric clash on opposite strands of the double helix (41, 58, 59). As a result, 5′-PyPu-3′ sequences within

the oligonucleotide represent positions where the largest helical distortions occur. Dickerson (41) has shown that these sequence-specific variations in the conformation of duplex DNA observed in the crystal structure of a 12-mer could be quantitatively predicted through a series of simple "Calladine rule" sum function relationships (42). Although as Dickerson has more recently noted, more recent crystal structures have not supported the earlier "Calladine rules" (63). A comparison of the theoretical helical twist angles predicted from "Calladine's Rules" and the helical twist obtained from the NOESY distance refined structures of the decamer at various stages of the refinement is shown in figure 9.

For the initial model built structure with no NOE constraints, no correlation existed between the two sets of helical twists (fig. 9A).

(In the initial model built Arnott B-DNA the helical twist values are equivalent for all base steps.) The calculated helix twist values for this NOESY distance-restrained (using the two-spin approximation distances) energy-minimized structure is shown in figure 9B. The correlation between calculated and predicted values are very poor (correlation coefficient between the Calladine rules and AMBER calculated helix twist values is a *negative 0.48*). However, NOESY distance-restrained molecular dynamics calculations generally show much better correlation of predicted and observed helical twist values (19, 64; see below). Molecular dynamics calculations should be better able to overcome small energy barriers (on the order of kT) that otherwise limit the ability of an energy minimization scheme to locate a global energy minimum. As shown in figure 9C the MORASS refined/restrained molecular dynamics calculations (45 ps) on the decamer duplex are better able to correctly match the predicted sequence-specific variation of helix twist. By using "high" simulation temperatures (298°K) and large "force constants" (20–40 kcal/mol/N) for the NOESY distance-restraints, in concert with the more accurate MORASS-refined distances, we are able to search for structures that better represent the "correct" solution conformation. It is clear that a better correlation (R = 0.65) now exists between the two sets of helical twist data (figure 9C).

The final distance-restrained structure significantly reproduces the theoretical "Calladine Rules" helical twist values. As shown by these and other results (19, 64) NOESY distances appear to be able to restrain the calculated structures to conformations that accurately reflect these sequence-specific variations in the local conformation of the DNA. Even distances derived from the two-spin approximation treatment of the NOESY data are accurate enough to reproduce these large local variations in structure.

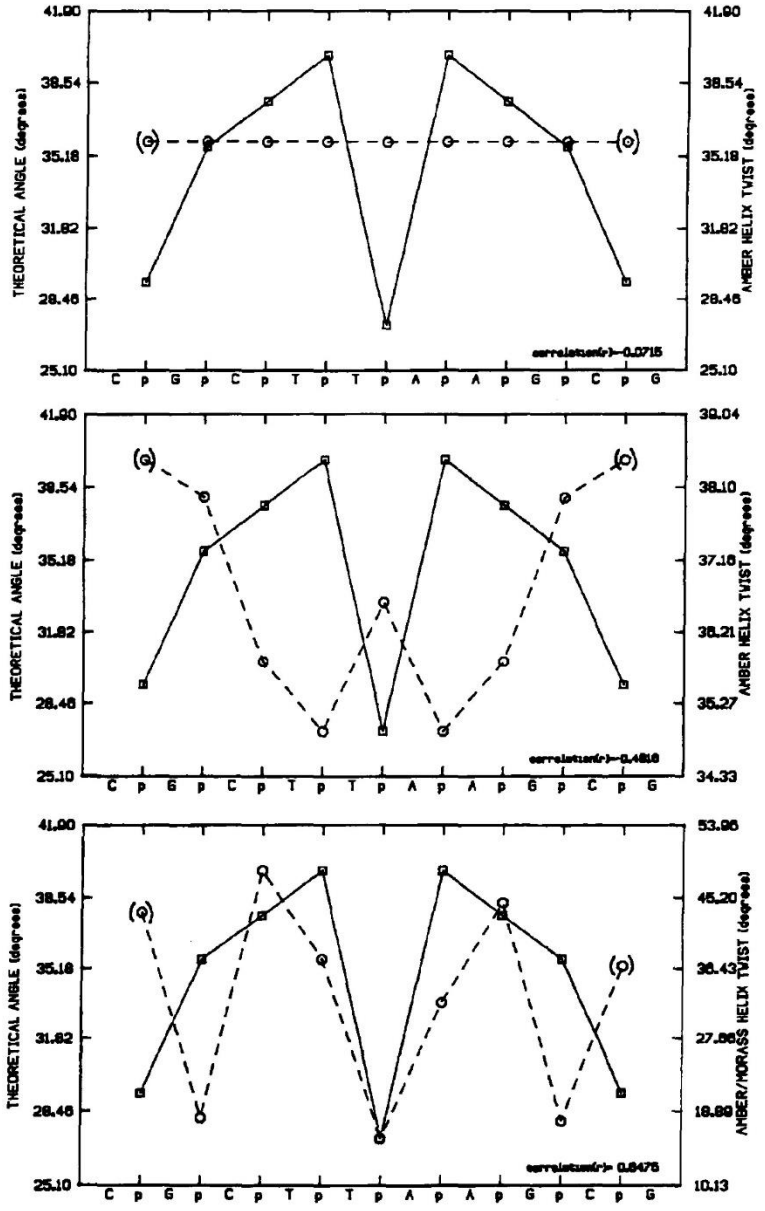

Figure 9. Predicted sequence-specific variations in the helix twist values for duplex decamer shown in figure 8 (solid curves calculated from helical twist sum function). Helix twist values derived from the final B-DNA(I) structure (dashed curves): (A) AMBER model built structure with uniform B-DNA 35.8° helix twist values for all base steps. (B) AMBER molecular mechanics calculated structures (no NOESY distance restraints) and the helix twist values for the final structure. (C) NOESY distance-restrained molecular mechanics calculated values for helix twist.

^{31}P Chemical Shifts as a Function of Sequence and Position

As discussed above, our laboratory has hypothesized that one of the major contributing factors which determines relative ^{31}P chemical shifts is the main chain torsional angles of the individual phosphodiester groups along the oligonucleotide double helix. Phosphates located toward the middle of a B-DNA double helix assume the lower energy, stereoelectronically (35) favored g^-, g^- conformation, while phosphodiester linkages located toward the two ends of the double helix tend to adopt a mixture of g^-, g^- and t, g^- conformations, where increased flexibility of the helix is more likely to occur. (The notation for the P–O ester torsion angles follows the convention of Seeman et al. (65) with the ζ, P–O-3′ angle given first followed by the α P–O-5′ angle.) Because the g^-, g^- conformation is responsible for a more upfield ^{31}P chemical shift, while a t, g^- conformation is associated with a lower-field chemical shift, internal phosphates in oligonucleotides would be expected to be upfield of those nearer the ends. Although several exceptions have been observed, this positional relationship appears to be generally valid for oligonucleotides where ^{31}P chemical shift assignments have been determined (7, 14, 38, 43, 44, 66). Thus, the ^{31}P chemical shifts of the phosphates should move upfield as the position of the phosphate moves toward the center of the helix, as is generally observed for the decamer (fig. 7).

^{31}P Chemical Shifts and Calladine's Rules

In addition to the "positional effect," in a number of sequences there appears to be a sequence-specific effect on ^{31}P chemical shifts as well. A modest correlation exists between the local helical parameters such as helix twist or roll and ^{31}P chemical shifts (36, 43–45). However, for the $(CGCTTAAGCG)_2$ decamer, little correlation exists between ^{31}P chemical shifts and the helical twist (or roll) for the terminal base pairs as calculated by "Calladine's Rules" (R = 0.15; fig. 7).

^{31}P Chemical Shifts and $J_{H3'-P}$ Coupling Constants

As previously described, the $J_{H3'-P}$ coupling constants for the two decamers were measured using the 2D heteronuclear selective J-resolved spectra. The $J_{H3'-P}$ coupling constants are plotted versus sequence at various temperatures for the decamer in figure 10. The coupling constants decrease generally for the more interior phosphate groups (fig. 7). This pattern collapses at higher temperatures. At 80° all of the coupling constants are nearly identical. At this temperature, the DNA is completely denatured and in a single-strand random coil.

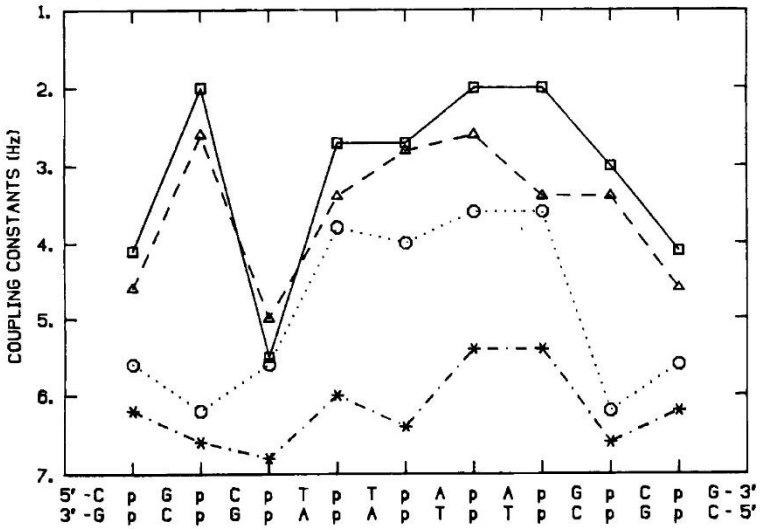

Figure 10. $J_{H3'-P}$ coupling constants are plotted versus sequence at various temperatures for the decamer. 18.5° (□), 30° (Δ). 50° (o), and 80°C (*).

It is important to note that ε and ζ torsional angle variations are highly correlated in B-DNA, with correlation coefficient of –0.92 (41, 58, 59) (the negative sign indicates that an increase in one angle decreases the other). In addition, α and γ torsional angle variations are also highly correlated in A-DNA, with a correlation coefficient also of –0.92 (67) (β is constrained to a trans conformation in both B-and A-DNA). As noted by Dickerson (41, 59) when the P–O3′ (ζ) conformation is g^-, invariably the C–O3′ conformation (ε) is found to be *t*. This ε(*t*), ζ(g^-) conformation is the most common backbone conformation (defined as the B_I(*t*,*g*) conformation) (41, 59). The other most common conformation for the (ε, ζ) pair is the (g^-, *t)* or B_{II} state. A "crankshaft" motion interconverts B_I and B_{II} conformations with only a modest movement of the phosphate. It is largely this variation in ε and ζ (as well as 8, 3, 36, 39, 62, 68) that allows the sugar phosphate backbone to "stretch" or "contract" to allow for variations in the local structure of B-DNA.

Thus these conformational changes may provide an explanation for much of the observed variation in ^{31}P chemical shifts and coupling constants.

The original correlation of ε and ζ torsional angles was based upon a limited comparison of several B DNA crystal structures (41, 59). As shown in figure 11, ε torsional angles were collected from 9 B-DNA crystal structures and plotted versus their corresponding ζ torsional angles. Again, a strong correlation (R = –0.86, ζ = –348.11–1.42ε) exists between the two torsional angles, confirming the previous relationship. Both B_I and B_{II} backbone conformations are observed in the B-DNA crystal structures as shown by the two relative clusters in the ε versus ζ plot of Figure ref 133. The B_{II} conformation is observed only in the terminal region (near the ends of the duplex) in the crystal structures. In solution the phosphates with small coupling constants correspond to a B_I conformation and those with a relatively large coupling constants correspond to a mixture of B_I and B_{II} conformations.

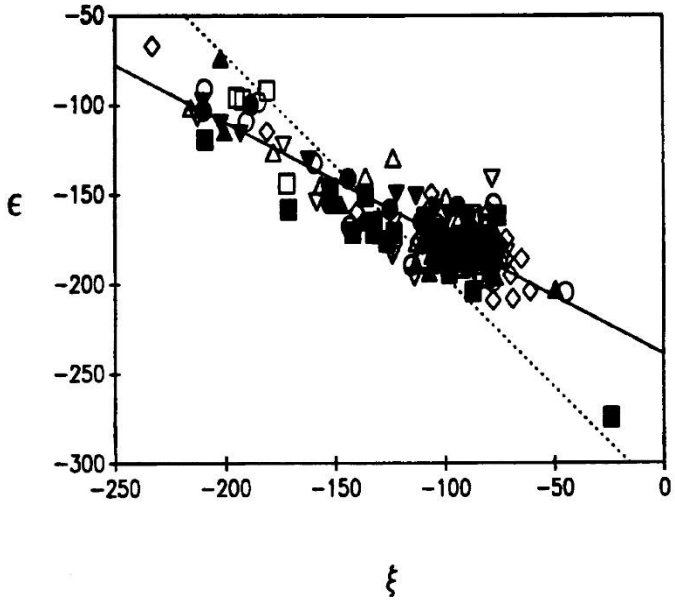

Figure 11. Plot of P–O3′ (ζ) vs. C3′–O3′ (ε) torsional angles for individual phosphates of B-DNA crystal structures. (•) dCGCGAATTCGCG, R.T.; 72; (▲) dCGCGAATTCGCG, 16K; 72; (▼) dCGCGAATTCGCG-cis-dichlorodiaminoplatinum (II); 72; (Δ), Bent dCG-CAATT^{Br}CGCG; 72; (o) Linear dCGCGAATT^{Br}CGCG; 72; (■) dCGCGAATTCGCG-Hoschst 33258; 73; (◊) dCGCGAATTTGCG; 74; (Δ) dCCAAGATTGG; 63; (▽) dGCGCGC 63. The best straight (solid) line is ζ = –367.5 – l.54ε, which differs slightly from that derived by Dickerson based upon just the 4 dodecamer structures (dashed line, ζ = –317–l.23ε).

The ^{31}P chemical shifts of the decamer are plotted versus the corresponding coupling constants in figure 12. It is clear that a significant correlation (R = 0.92) exists between $J_{H3'-P}$ and ^{31}P chemical shifts for the decamer. As described in references 68 and 39, this relationship is further substantiated by a combined plot of all the ^{31}P chemical shifts—$J_{H3'-P}$ coupling constants for 11 sequences analyzed in our laboratory (correlation coefficient of 0.82).

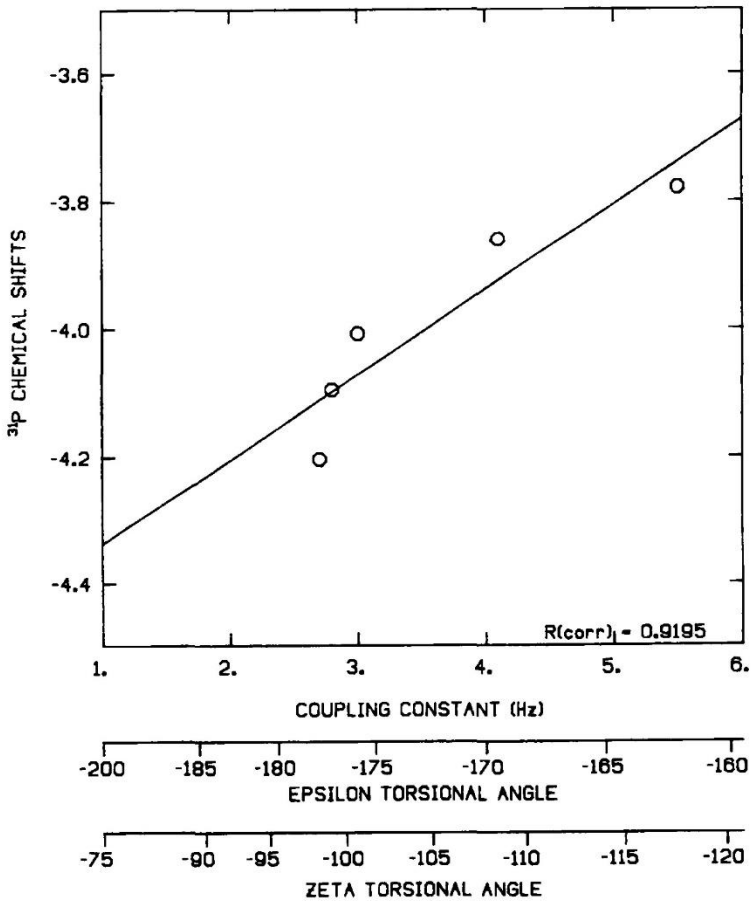

Figure 12. Correlation of ^{31}P chemical shifts (l8°C) with experimentally determined J(H3′–P) coupling constants (1st X-axis), calculated ε (2nd X-axis), and ζ torsional angles (3rd X-axis).

Time Course for Backbone Torsional Angle Variations from Restrained Molecular Dynamics Calculations

The analysis of helical twist variation from the NOESY distance-restrained structures established the ability of the NOE data to reproduce the sequence-specific variations in local helical parameters such as the "Calladine Rules." However, $^{1}H/^{1}H$ 2D NOESY spectra give no direct information on the sugar phosphate conformation and NOESY distance-restrained structures have been suggested to be effectively disordered in this part of the structure (4). The measured ^{31}P chemical shifts and $J_{H3'-P}$ coupling constants demonstrate clearly that the backbone is not disordered but shows similar sequence and position specificity (as well as site specificity—see ref. 39). As shown in figure 13, the restrained molecular dynamics calculations are able to reproduce the observed variation in the ε torsional angles for the decamer and rather accurately parallel the variation in ^{31}P chemical shifts and $J_{H3'-P}$ coupling constants.

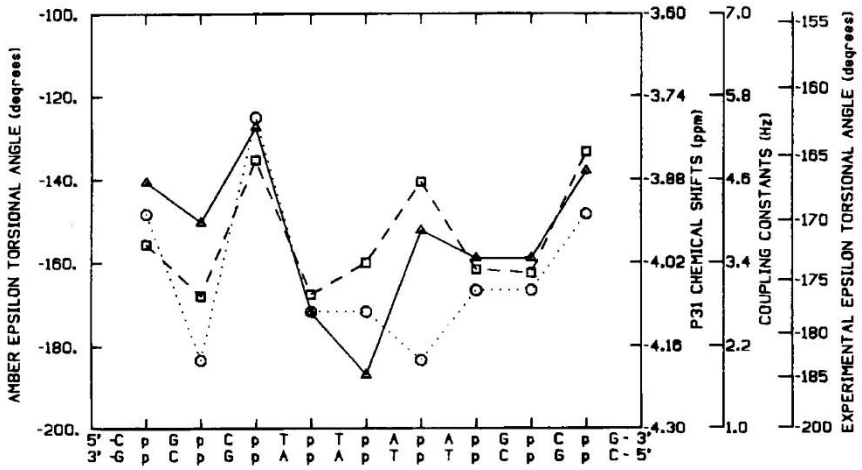

Figure 13. Plot of ^{31}P chemical shifts (–Δ–)and P-H3′ coupling constants (· · o · ·) vs. sequence for d(CGCTTAAGCG). The calculated ε torsional angles (--□--) derived by averaging the entire 45 ps time course for the restrained molecular dynamics refinement is also shown.

The ε torsional angles were measured from either the final hybrid matrix/MORASS/restrained MD structure of the decamer or averaged over the entire 45 ps dynamics of the refinement (shown in fig. 13). The ε torsional angles derived from the MD simulations are plotted as a function of sequence in figure 13. With the exception of the ε torsional angle for A6pA7, it is clear that a strong correlation exists between the pattern of the variation of the torsional angles derived from the restrained MD calculations and the experimentally measured coupling constants. These results provide further support to the reliability of the MORASS/restrained MD refinement methodology to accurately reproduce the solution structure.

The origin of the sequence-specific variation of the backbone conformation derived from the restrained molecular dynamics refinement is reflected in the time course of the six backbone torsional angles, α–ζ (P^{α}–O5′$^{\beta}$–C5′$^{\gamma}$–C4′$^{\delta}$–C3′$^{\varepsilon}$–O3′$^{\zeta}$–P) of a representative A17 residue on the 3′-strand (fig. 14).

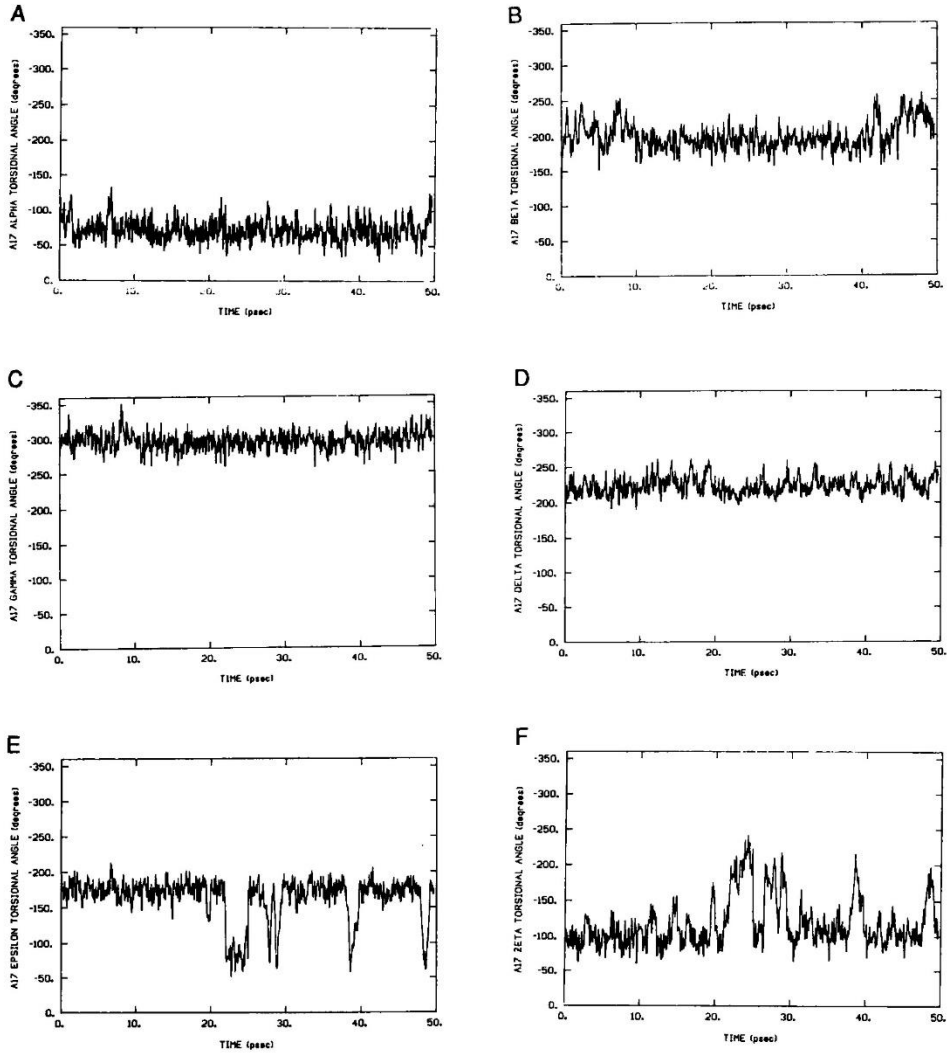

Figure 14. Time course for the fluctuations in the backbone torsional angles for the A17 residue during the restrained molecular dynamics refinement (A) α, (B) β, (C) γ, (D) δ, (E) ε, and (F) ζ.

Most of these torsional angles showed relatively small amplitude fluctuations about the average B-DNA values for the 45 ps restrained molecular dynamics calculation. As noted from X-ray studies (41, 59) of B-DNA the ε and ζ torsional angles show the largest variability and indeed our calculations demonstrate that large amplitude fluctuations occur for these two torsional angles. These torsional angle changes reflect a transition from the low energy B_I conformation to the higher energy B_{II} conformation. These transitions were short-lived and relaxed back to the low-energy conformation. These calculations also provided strong support for the crankshaft conformational transition between the B_I and B_{II} conformations and the strong correlation between the ε and ζ torsion angles observed in the X-

ray crystal structures of B-DNA (41, 59). The correlation between the ε and ζ torsion angles over the entire 45 ps restrained MD time course for the A17 phosphate on the 3′-strand of the decamer is shown in figure 15.

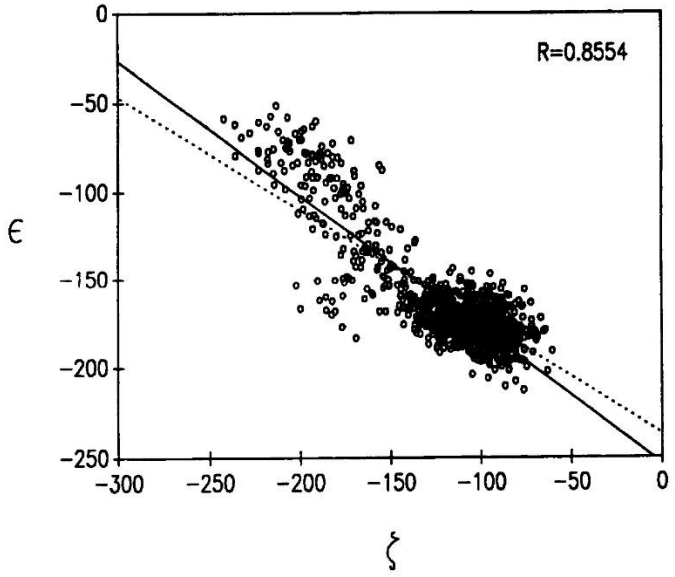

Figure 15. Plot of P-O3′ (ζ) vs. C3′-O3′ (ε) torsional angles for the A17 residue during the 45 ps restrained molecular dynamics refinement. ζ/ε torsional angles were obtained for the phosphate every 50 fs. The best straight (solid) line is $\zeta = -348.1 - 1.42\varepsilon$ (R = 0.86). The dashed line is derived from the crystal structures from figure 11 ($\zeta = -367.5 - 1.54\varepsilon$).

The similarity between the plots of figures 11 (based upon the crystal structures) and 15 (based upon the solution structure derived from NOESY restraining distances in the gas-phase MD calculation) is particularly striking. The ability of the restrained MD calculation to reproduce these variations provides further support for the validity of these NOESY distance-restrained refinement procedures.

NMR studies have suggested that the duplex conformation in solution may not be identical to the static picture provided by X-ray diffraction in the crystal state (20, 30). This has raised the question whether some of the sequence-specific structural variations observed in the X-ray crystallographic studies are the result of less profound crystal packing forces (69, 70). Indeed Dickerson et al. (70) have suggested that all of the sequence-specific variation in the B_I and B_{II} conformations arises from crystal packing forces. Similar conclusions have been reached in a Raman spectroscopy analysis of the backbone phosphate conformation in solution and the solid state (71). Our own results clearly show that there are significant variations (sequence- and/or position-dependent) in the relative populations of the B_I and B_{II} conformations in duplex oligonucleotides in solution. This variation in the backbone conformation does not readily follow any simple Calladine-type rules. In the Dickerson et al. (70) analysis variation in local helix parameters such as helix twist, base roll, propeller twist, and sugar pucker are determined by base sequence and thus are

"hard" parameters and a real phenomenon. They further argue that the backbone conformation is a "soft" parameter that is easily perturbed by crystal packing forces and is "an epiphenomenon." Our own results confirm their conclusions regarding the crystal state. However, in solution the backbone conformation clearly does display sequence-, position-, and site-specificity (see also 36, 39, 68) and as such these variations indeed represent true "phenomena."

Origin of Sequence-Specific Variation in the ε and ζ, Torsional Angles and P-H3′ Coupling Constants; C4′-C4′ Inter-residue Distances

As noted earlier, the possible basis for the sequence- and position-specific variation in the backbone conformation can be analyzed in terms of deoxyribose phosphate backbone distortions arising from local variations of the helical parameters and geometry. Thus, according to the Calladine rules, decreasing the helical twist angle t_g reduces the steric clashing in the minor groove in a 5′-Py-Pu-3′ sequence by pulling the N-2 and N-3 atoms of the purines farther apart. As the helix unwinds (and the helix twist t_g decreases), the length of the deoxyribose phosphate backbone decreases (3, 36, 68). These local helical changes require changes in the deoxyribose phosphate backbone angles α–ζ.

As the helix winds or unwinds, our laboratory has shown (36) that the distance between the adjacent C-4′ atoms of deoxyribose rings along an individual strand ($D_{4'4'}$) must change to reflect the stretching and contracting of the deoxyribose phosphate backbone between the two stacked base pairs. To a significant extent, these changes in the overall length of the deoxyribose phosphate backbone "tether" are reflected in changes in the P-O ester (as well as other) torsional angles.

The observed variations in the P-O (and C-O) torsional angles may provide the linkage between the positional and Calladine rule–type sequence-dependent structural variations in the duplex and the ^{31}P chemical shifts and coupling constants.

Significantly, the $D_{C4'C4'}$ distances obtained from the four crystal structures (41, 58, 59) of a dodecamer as well as the calculated $D_{C4'C4'}$ distances of the decamer also follow a similar change as a function of t_g, as shown in figure 16.

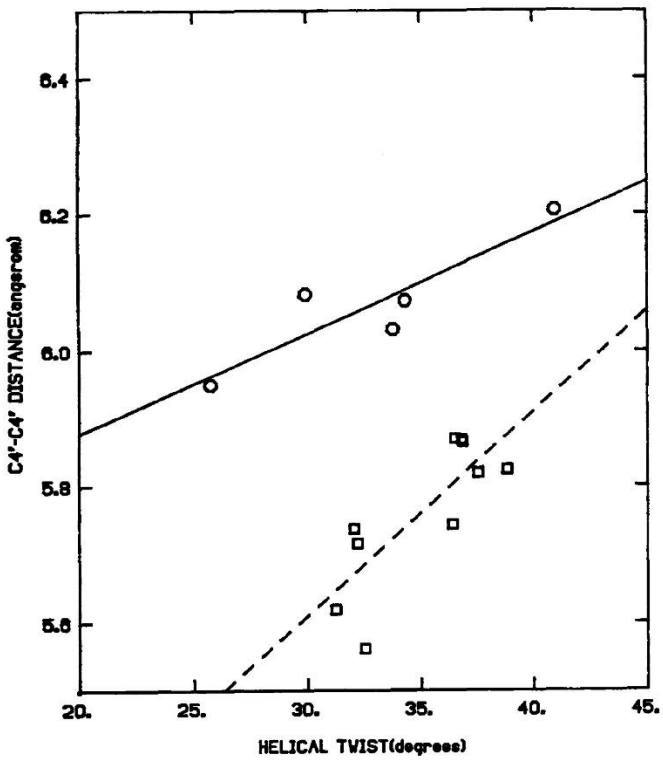

Figure 16. Correlation of distance between adjacent deoxyribose C4′ atoms, $D_{C4'C4'}$, along one strand of duplex oligonucleotide and helical twist parameter t_g derived from the solution structure B-DNA (I) 9th iteration for the decamer (o; solid line) and the crystal structure of the dodecamer d(CGCGAATTCGCG) (--□--). Values for the decamer were derived by averaging the entire 45 ps time course for the restrained molecular dynamics refinement. The values for the dodecamer are based upon the four crystal structures. The crystallographic data includes only B_I conformations, and the residue at the ends of the duplex has been eliminated. Each conformation represents the average of phosphate conformations on complementary strands and has also been end-for-end averaged.

The correlation coefficient between the crystallographically derived $D_{C4'C4'}$ distances and t_g is a quite respectable value of 0.77 (fig. 16). While the restrained MD calculated distances for the decamer are shifted slightly from the crystal structure distances, the trend is quite similar and the correlation is very good (R = 0.90).

A remarkable, similar correlation also exists between the $J_{H3'-P}$ coupling constant and the calculated C4′-C4′ distances derived from the NOESY distance-restrained MD MORASS refined structure for the decamer (R = 0.69; fig. 17). Figure 17 also demonstrates that there is a good correlation between the derived ε torsion angles from the MORASS/MD refinement and C4′-C4′ distances (R = 0.83).

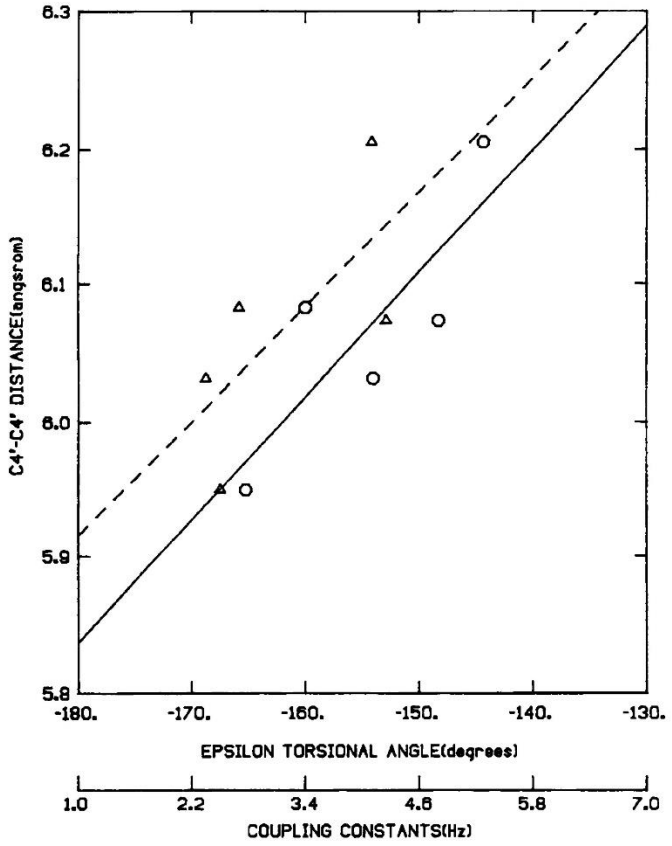

Figure 17. Plot of distance between adjacent deoxyribose C4′ atoms, $D_{C4'C4'}$ along one strand of the decamer vs. measured P-H3′ coupling constant (Δ; dashed line) and the calculated ε torsional angles (o; solid line) derived by averaging the entire 45 ps time course for the restrained molecular dynamics refinement for the decamer d(CGCTTAAGCG).

The C4′-C4′ distances were double averaged to remove any anomalous effects such as base-pair sliding out of the helix (see legend fig. 16). The ε torsional angles have been calculated by averaging all of the values taken every 50 fs in the entire 45 ps NOESY distance-restrained MORASS refinement.

Conclusion

These results provide strong support for our hypothesis that variations in the backbone torsional angles are largely responsible for ^{31}P chemical shift variations in duplex oligonucleotides. This analysis was verified by the strong correlation of ^{31}P chemical shifts with $J_{H3'-P}$ coupling constants, which in turn relates ^{31}P chemical shifts to ε (and indirectly to ζ) torsional angles through a modified Karplus equation.

Most importantly, calculated torsional angles from ^{31}P chemical shifts and $J_{H3'-P}$ coupling constants and molecular dynamics calculations do not always agree with the Calladine

rules derived from analysis of duplex crystal structures. Thus while local base-pair geometry and helical parameters can be reproduced by the Calladine rules, the relationship between sequence/position-specificity and backbone geometry appears to be more complex. As seen in the time course of the fluctuations in the phosphate ester conformation (fig. 14), rapid crankshaft conformational transitions occur on the ps timescale. Presumably the crystal structure represents a single "snapshot" of one of these time frames, catching the phosphate in a B_I, B_{II}, or intermediate conformational state (probably closer analysis of the thermal parameters would reveal significant disorder of the phosphates).

We now believe that our hybrid matrix/MORASS/restrained molecular dynamics procedure is providing highly refined structures that accurately reproduce not only the overall solution conformation but the sugar phosphate backbone conformation as well. As shown in figure 13, there is a strong correlation between the measured $J_{H3'-P}$ coupling constants and ^{31}P chemical shifts. Most importantly, we have used our hybrid matrix/MORASS/restrained molecular dynamics refinement to calculate the average ε torsional angle for the individual phosphates from the 45 ps of restrained molecular dynamics refinement of the NOESY-derived distances. The phosphate undergoes concerted crankshaft jumps between the B_I and B_{II} conformational states during these simulations and yet as shown in figures 13 and 17, the average ε torsional angle very much fits the torsional angle derived from either the coupling constant or ^{31}P chemical shift data. These results provide the most striking arguments in support of our theory as well as validating the hybrid matrix/MORASS/restrained molecular dynamics procedure.

Acknowledgments – Supported by NIH (AI27744); the Purdue University Biochemical Magnetic Resonance Laboratory, which is supported by NIH (grant RRO 1077 from the Biotechnology Resources Program of the Division of Research Resources); the NSF National Biological Facilities Center on Biomolecular NMR, Structure, and Design at Purdue (grants BBS 8614177 and 8714258 from the Division of Biological Instrumentation); and the National AIDS Research Center at Purdue (AI727713). We greatly appreciate the contributions of Robert Meadows, James Metz, Edward Nikonowicz, Dr. Julian Tirado-Rives, and Dr. Robert Santini.

Note

1. Gauche(–) or –60° torsional angle; trans or 180° torsional angle. Crystal structures of duplex oligonucleotides show that these angles are only approximate and indeed the ζ angle is generally closer to –90° for what we define as "g^-".

References

1. B. R. Reid, *Quart. Rev. Biophys. 20*, 1–34 (1987).
2. D. J. Patel, L. Shapiro, and D. Hare, *Q. Rev. Biophys. 20,* 35–112 (1987).
3. D. G. Gorenstein, R. P. Meadows, J. T. Metz, E. Nikonowicz, and C. B. Post, *Advances in Biophysical Chem.*", in press, 1990.
4. F. J. M. Van De Ven and C. W. Hilbers, *Eur. J. Biochem. 178*, 1–38 (1988).
5. J. Feigon, W. Leupin, W. A Denny, and D. R. Keams, *Biochemistry 22*, 5930–5942; 5943–5951 (1983).

6. D. R. Hare, D. E. Wemmer, S. H. Chou, G. Drobny, and B. Reid, *J. Mol. Biol. 171*, 319 (1983).
7. S. A. Schroeder, J. M. Fu, C. R. Jones, and D. G. Gorenstein, *Biochemistry 26*, 3812–3821 (1987).
8. D. R. Kearns, *Crit. Rev. Biochem. 15*, 237–290 (1984).
9. T. L. James, *Phosphorus-31 NMR: Principles and Applications* (D. Gorenstein, ed.), 349–400, Academic Press, Orlando, 1984.
10. D. Frechet, D. M. Cheng, L.-S. Kan, and P. O. P. Ts'o, *Biochemistry 22*, 5194–5200 (1983).
11. G. Gupta, M. H. Sarma, and R. H. Sarma, *Biochemistry 27*, 7909–7919 (1988).
12. M. A Broido, G. Zon, and T. L. James, *Biochem. Biophys. Res. Commun. 119*, 663–670 (1984).
13. R. M. Scheek, R. Boelens, N. Russo, J. H. Van Boom, and R. Kaptein, *Biochemistry 23*, 1371–1376 (1984).
14. S. Schroeder, C. Jones, J. Fu, and D. G. Gorenstein, *Bull. Magn. Reson. 8*, 137–146 (1986).
15. T. F. Havel, I. D. Kuntz, and G. M. Crippen, *Bull. Math. Biol. 45*, 665–720 (1983).
16. W. Braun and N. Go, *J. Mol. Biol. 186*, 613–621 (1983).
17. K. Wuthrich, *NMR of Proteins and Nucleic Acids*, Wiley, New York, NY, 1986.
18. E. Zuiderweg, R. Scheek, R. Boelens, W. Gunsteren, and R. Kaptein, *Biochemie 67*, 707–715 (1985).
19. M. Nilges, G. M. Clore, A. M. Gronenborn, N. Piel, and L. W. McLaughlin, *Biochemistry 26*, 3734–3744 (1987).
20. E. Nikonowicz, R. Meadows, and D. G. Gorenstein, *Biochemistry 29*, 4193–4206 (1990).
21. G. M. Clore and A. M. Gronenborn, *J. Magn. Reson. 61*, 158–164 (1985).
22. J. W. Keepers and T. L. James, *J. Magn. Res. 57*, 404–426 (1984).
23. A. A. Bothner-by and J. H. Noggle, *J. Am. Chem. Soc. 101*, 5152–5155 (1979).
24. E. T. Olejniczak, R. T. Gampe, and S. W. Fesik, *J. Magn. Reson.* 67, 28 (1986).
25. G. Lancelot, J.-L. Guesnet, and F. Vovelle, *Biochemistry 28*, 7871–7878 (1989).
26. R. Boelens, T. M. G. Koning, and R. Kaptein, *J. Mol. Struc. 173*, 299–311 (1988).
27. R. Boelens, T. M. G. Koning, G. A. van der Marel, J. H. van Boom, and R. Kaptein, *J. Magn. Reson. 82*, 290–308 (1989).
28. E. Nikonowicz, R. Meadows, C. Post, C. Jones, and D. G. Gorenstein, *Bull. Magn. Reson. 11*, 226–229 (1989).
29. D. G. Gorenstein, *Phosphorus-31 NMR: Principles and Applications* (D. G. Gorenstein, ed.), Academic Press, New York, 1984.
30. V. Sklenár, H. Miyashiro, G. Zon, H. T. Miles, and A. Bax, *FEBS letters 208*, 94–98 (1986).
31. J. M. Fu, S. A. Schroeder, C. R. Jones, R. Santini, and D. G. Gorenstein, *J. Magn. Reson*. *77*, 577–582 (1988).
32. C. R. Jones, S. A. Schroeder, and D. G. Gorenstein, *J. Magn. Reson. 80*, 370–374 (1988).
33. D. G. Gorenstein, *Annu. Rev. Biophys. Bioeng. 10*, 355 (1981).
34. D. G. Gorenstein and J. B. Findlay, *Biochem. Biophys. Res. Commun. 72*, 640 (1976).
35. D. G. Gorenstein, *Chem. Rev. 87*, 1047–1077 (1987).
36. D. G. Gorenstein, S. A. Schroeder, J. M. Fu, J. T. Metz, V. A. Roongta, and C. R. Jones, *Biochemistry 27*, 7223–7237 (1988).
37. D. G. Gorenstein, *Prog. NMR Spectrosc. 16*, 1–98 (1983).
38. D. G. Gorenstein, J. B. Findlay, R. K. Momii, B. A Luxon, and D. Kar, *Biochemistry 15*, 3796–3803 (1976).
39. V. A. Roongta, C. R. Jones, and D. G. Gorenstein, *Biochemistry 29*, 5245–5258 (1990).

40. B. A. Connolly and F. Eckstein, *Biochemistry 23*, 5523–5527 (1984).
41. R. E. Dickerson, *J. Mol. Biol. 166*, 419–441 (1983).
42. C. R. Calladine, *J. Mol. Biol. 161*, 343–352 (1982).
43. J. Ott and F. Eckstein, *Biochemistry 24*, 253 (1985).
44. J. Ott and F. Eckstein, *Nucleic Acids Res.* 13, 6317–6330 (1985).
45. E. Ragg, R. Mondelli, A Garbesi, F. P. Colonna, C. Battistini, and S. Vioglio, *Magn. Reson. Chem. 27*, 640–646 (1989).
46. C. B. Post, R. Meadows, and D. G. Gorenstein, *J. Am. Chem. Soc.*, in press (1990).
47. D. O. Shah, K. Lai, and D. G. Gorenstein, *J. Am. Chem. Soc. 106*, 4302 (1984).
48. D. O. Shah, K. Lai, and D. G. Gorenstein, *Biochemistry 23*, 6717–6723 (1984).
49. D. J. States, R. A. Haberkorn, and D. J. Rueben, *J. Magn. Reson. 48*, 286–292 (1982).
50. U. Piantini, O. W. Sorensen, and R. R. Ernst, *J. Am. Chem. Soc. 104*, 6800–6801 (1982).
51. H. Kessler, C. Griesinger, J. Zarbock, and H. R. Loosli, *J. Magn. Reson. 57*, 331–336 (1984).
52. V. Sklenar and A Bax, *J. Am. Chem. Soc. 109*, 7525–7526 (1987).
53. P. P. Lankhorst, C. A. G. Haasnoot, C. Erkelens, and C. Altona, *J. Biomol. Struct. Dyn. I*, 1387–1405 (1984).
54. P. K. Weiner and P. A. Kollman, *J. Comp. Chem. 2*, 287–303 (1981).
55. T. E. Ferrin and Langridge, *Computer Graphics 13*, 320 (1980).
56. R. Powers, R. K. Olsen, and D. G. Gorenstein, *J. Biomol. Struct. Dyn. 7*, 515–556 (1989).
57. R. Meadows, C. Post, and D. G. Gorenstein, MORASS *Program*, (1989).
58. W. Saenger, *Principles of Nucleic Acid Structure*, Springer-Verlag, New York, 1984.
59. R. E. Dickerson and H. R. Drew, *J. Mol. Biol. 149*, 761–786 (1981).
60. G. C. Levy, D. J. Craik, A. Kumar, and R. E. London, *Biopolymers 22*, 2703–2726 (1983).
61. P. N. Borer, N. Zanatta, T. A. Holak, G. C. Levy, J. H. van Boom, and A. H.-J. Wang, *J. Biomol. Struct. Dyn. 6*, 1373–1386 (1984).
62. E. Nikonowicz, V. Roongta, C. R. Jones, and D. G. Gorenstein, *Biochemistry 28*, 8714–8725 (1989).
63. G. G. Prive, U. Heinemann, S. Chandrasegaran, L. Kan, M. L. Kopka, and R. E. Dickerson, *Science 238*, 498–504 (1987).
64. J.-F. Lefevre, A. N. Lane, and O. Jardetzky, *Biochemistry 26*, 5076–5090 (1987).
65. N. C. Seeman, J. M. Rosenberg, F. L. Suddath, J. J. Park Kim, and A. Rich, *J. Mol. Biol. 104*, 142–143 (1976).
66. D. G. Gorenstein, *Jerusalem Symposium, NMR in Molecular Biology* (B. Pullman, ed.), 1–15, D. Reidel Publishing Co., 1978.
67. Z. Shakked and D. Rabinovitch, *Prog. Biophys. Molec. Biol. 47*, 159–195 (1986).
68. S. A. Schroeder, V. Roongta, J. M. Fu, C. R. Jones, and D. G. Gorenstein, *Biochemistry 28*, 8292–8303 (1989).
69. S. Jain and M. Sundaralingam, *J. Biol. Chemistry 264*, 12780–12784 (1989).
70. R. E. Dickerson, D. S. Goodsell, M. L. Kopka, and P. E. Pjura, *J. Biomol. Struct. Dyn. 5*, 557–579 (1987).
71. J. M. Benevides, A. H.-J. Wang, G. A. van der Marel, J. H. van Boom, and G. J. Thomas Jr., *Biochemistry 27*, 931–938 (1988).
72. F. A. Jurnak and A. McPherson, *Biological Macromolecules and Assemblies*, 471–494, John Wiley and Sons, New York, 1984.

73. P. E. Pjura, K. Grezeskowiak, and R. E. Dickerson, *J. Mol. Biol.* 197, 257–271 (1987).
74. W. N. Hunter, T. Brown, G. Kneale, N. N. Anand, D. Rabinovich, and O. Kennard, *J. Biol. Chem. 262*, 9962–9970 (1987).